Computers and Electronics in Agriculture 237 (2025) 110523

Contents lists available at ScienceDirect

Computers and Electronics in Agriculture

journal homepage: www.elsevier.com/locate/compag

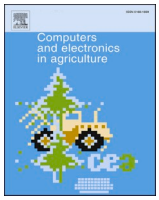

Precision monitoring of rice nitrogen fertilizer levels based on machine learning and UAV multispectral imagery☆

Ming-Der Yang [a,b,e], Yu-Chun Hsu [c,*], Yi-Hsuan Chen [a,b], Chin-Ying Yang [b,d,e], Kai-Yun Li [f,g]

[a] Department of Civil Engineering, and Innovation and Development Center of Sustainable Agriculture, National Chung Hsing University, Taichung 40227, Taiwan
[b] Smart Sustainable New Agriculture Research Center (SMARTer), Taichung 40227, Taiwan
[c] Department of Urban Design and Sustainable Development, Ming Chuan University, Taoyuan 33348, Taiwan
[d] Department of Agronomy, National Chung Hsing University, Taichung 40227, Taiwan
[e] Innovation and Development Center of Sustainable Agriculture (IDCSA), National Chung Hsing University, Taichung 40227, Taiwan
[f] Institute of Agriculture and Environmental Sciences, Estonian University of Life Sciences, Kreutzwaldi 5, 51006 Tartu, Estonia
[g] Eawag, Swiss Federal Institute of Aquatic Science and Technology, Department Water Resources and Drinking Water, 8600 Dübendorf, Switzerland

ARTICLE INFO

Keywords:
Nitrogen fertilizer monitoring
Machine learning
Multispectral imagery
Feature selection
Precision agriculture

ABSTRACT

Rice is the primary food crop globally, and effective nitrogen fertilizer management is essential for optimizing yield while minimizing environmental impact. This study integrated unmanned aerial vehicle (UAV) imagery with multispectral imaging and machine learning (ML) methods to classify nitrogen levels (N levels) in rice fields. Experimental fields with various N levels (underfertilized, optimal fertilization, and overfertilized) were imaged in 2020 and 2021 by using UAVs. The captured images underwent geometric and spectral corrections, and rice pixel segmentation was performed using a decision tree classifier, which achieved a recall of 95.3 % and an overall accuracy of 88.8 %. N level classification was performed by extracting 16 spectral and structural features from the images, including color space transformations, vegetation indices, and canopy coverage. These features were input to support vector machine (SVM) and *k* nearest neighbors (KNN) models, and feature selection methods were applied to improve performance. The SVM model outperformed the KNN model, particularly in Period II, achieving an overall accuracy of 90.0 % when the chi-square feature selection method was applied. The Red Edge Ratio Vegetation Index and canopy coverage were the most informative features for classification. The integration of UAV-based multispectral imagery and ML in this study enhanced nitrogen classification accuracy and scalability. The method provides a data-driven approach for precision agriculture and sustainable fertilization management.

1. Introduction

Rice (*Oryza sativa* L.) is a staple food crop worldwide. Taiwan's average annual rice production from 2016 to 2020 reached approximately 1.7 million tons across 270,000 ha (Taiwan Council of Agriculture, 2020). Nitrogen is an essential macronutrient that plays a critical role in rice growth and yield. It is often supplemented through fertilization, but inefficient fertilization remains a key challenge in modern rice cultivation. Although nitrogen application is necessary for increasing productivity, improper (deficient or excess) fertilization can have negative agronomic and environmental consequences. Nitrogen deficiency reduces chlorophyll synthesis, leading to stunted growth and lower yields. Overfertilization increases the risks of eutrophication, soil acidification, pest infestations, and structural weaknesses in rice plants, which increase the susceptibility of the plants to lodging under strong winds or rain (Yang et al., 2020). A study investigated fertilizer application intervals for rice and revealed a close relationship between lodging and cultivation conditions (Wu et al., 2022). Conventional nitrogen management strategies are based on fixed schedules or visual assessments, but these methods lack precision or are not adaptable to variations in field conditions. Accordingly, advanced monitoring techniques are necessary for improved decision-making.

Traditionally, farmers assess nitrogen status on the basis of their empirical judgment and leaf color charts (LCCs). LCCs provide a visual

☆ This article is part of a special issue entitled: 'Precision Nutrient Management' published in Computers and Electronics in Agriculture.

* Corresponding author.
E-mail addresses: mdyang@nchu.edu.tw (M.-D. Yang), bigq@mail.mcu.edu.tw (Y.-C. Hsu), emiyang@dragon.nchu.edu.tw (C.-Y. Yang), kai-yun.li@eawag.ch (K.-Y. Li).

https://doi.org/10.1016/j.compag.2025.110523
Received 30 December 2024; Received in revised form 4 May 2025; Accepted 6 May 2025
Available online 12 May 2025

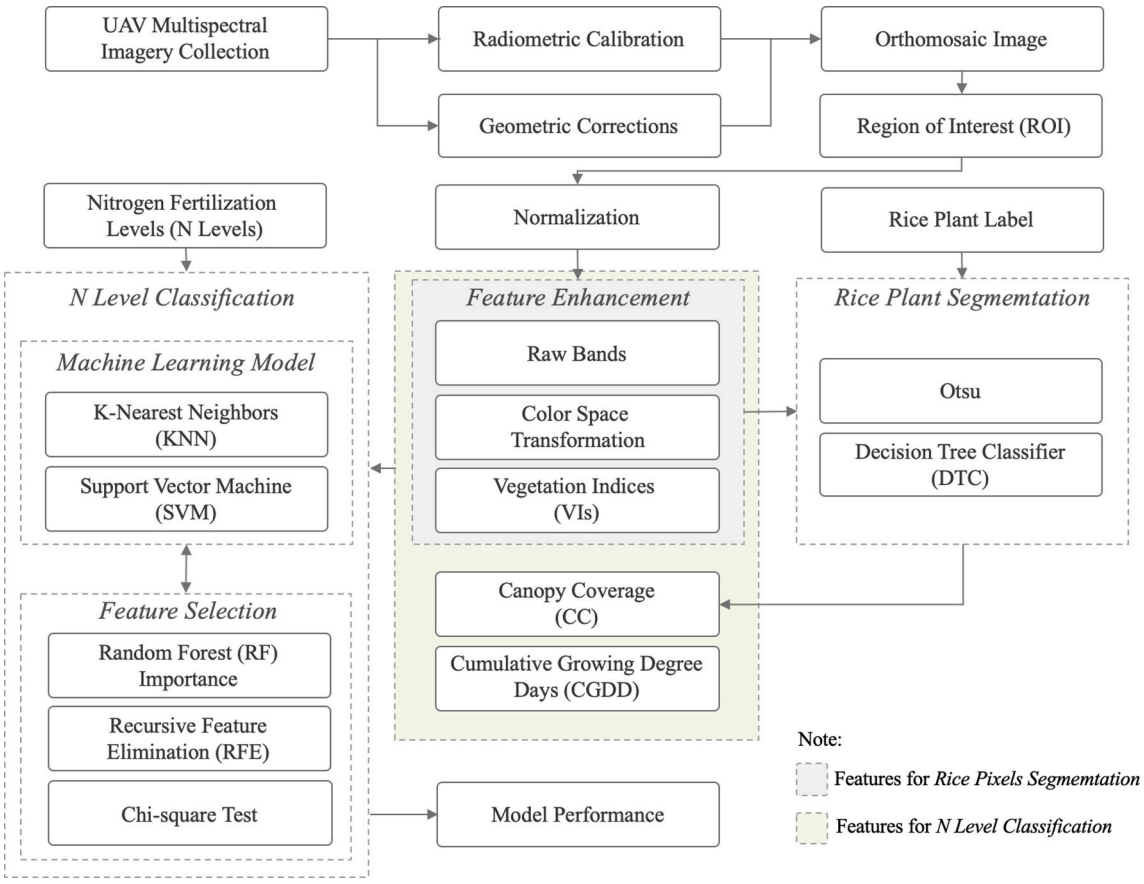

Fig. 1. Workflow of the UAV multispectral imagery-based N level classification framework. UAV images undergo radiometric calibration and geometric corrections to build orthomosaic images, from which the ROI is extracted and normalized. Rice plant segmentation is performed using Otsu and DTC. Feature enhancement integrates raw bands, color space transformations, VIs, CC, and CGDD. Feature selection methods, including RF Importance, RFE, and the Chi-square Test, refine features for N level classification using KNN and SVM.

reference for estimating chlorophyll content and adjusting fertilization accordingly (Haboudane et al., 2002). However, these methods are inherently subjective; assessments vary owing to differences in perception between individuals, lighting conditions, and experience levels, all of which can lead to inconsistent nitrogen application (Wang et al., 2018). Moreover, LCCs and subjective assessments provide broad indications of nitrogen status but are limited in their ability to adapt to real-time field conditions or capture intra-field spatial variability; consequently, they often result in over- or under-fertilization (Li et al., 2014). LCC-based assessments are also only broad indicators; they are inferior to precise nitrogen quantification and insufficient for implementing site-specific fertilization strategies (Orillo et al., 2014). Scalable and data-driven monitoring solutions could overcome these limitations and support precise nitrogen management.

As agricultural workforces age and labor shortages increase, digital tools and automation have become crucial for improving farm management and efficiency. In recent years, machine learning (ML) techniques have been increasingly applied for precision agriculture. These techniques can enhance crop growth monitoring, optimize fertilization, and improve yield predictions. For example, Tseng et al. (2022) employed ML models to monitor seedling growth, and Yang et al. (2021, 2025a) and Brinkhoff et al. (2025) developed spectral and multispectral prediction frameworks for optimizing rice harvest timing. In the context of nitrogen management, supervised learning models have demonstrated promise for classifying nitrogen levels (N levels) on the basis of the spectral characteristics of leaf images. Wang et al. (2018) classified nitrogen content in hyperspectral tea leaf images by using support vector machine (SVM) and extreme learning machine models; a comparison of the models indicated that the SVM model had superior performance in preventing over- or under-fertilization. Orillo et al. (2014) used a multilayer perceptron (MLP) to classify the nitrogen content in rice leaves by comparing visible-light sample images with LCCs to optimize nitrogen application and improve yield. However, these models require high-quality image data, necessitating the use of remote sensing for data collection.

Recent advancements in unmanned aerial vehicle (UAV)-based remote sensing have transformed precision agriculture, enabling high-resolution, real-time monitoring of crop health and fertilization needs. Researchers have combined multispectral UAV imagery with deep learning, object detection, and semantic segmentation techniques to optimize fertilization strategies and yield estimation; for example, these techniques have been used to determine broccoli harvest timing (Lee et al., 2023). These techniques offer greater flexibility and precision than traditional single-point sampling, which is impractical for assessing the spatial variability in a field. Compared with aerial and satellite imaging, UAV-based imaging provides higher-resolution data and more granular site-specific monitoring. Hence, UAVs constitute an ideal tool for large-scale nitrogen assessment (Yang et al., 2021). Chlorophyll concentration, an indicator of N levels, can be estimated through remote sensing (Yang et al., 2000). Some traditional VIs, such as the Normalized Difference Vegetation Index (NDVI), are less effective for estimating the nitrogen content of dense canopies.

To improve the nitrogen classification accuracy of UAV-based monitoring, current methods often integrate spectral, textural, and structural features (Liu et al., 2023). Measuring structural attributes, such as canopy volume weighted by color parameters, can also enhance biomass estimation (Liu et al., 2024). In this study, UAV imagery was used to assess N levels. To ensure accuracy, precise image preprocessing

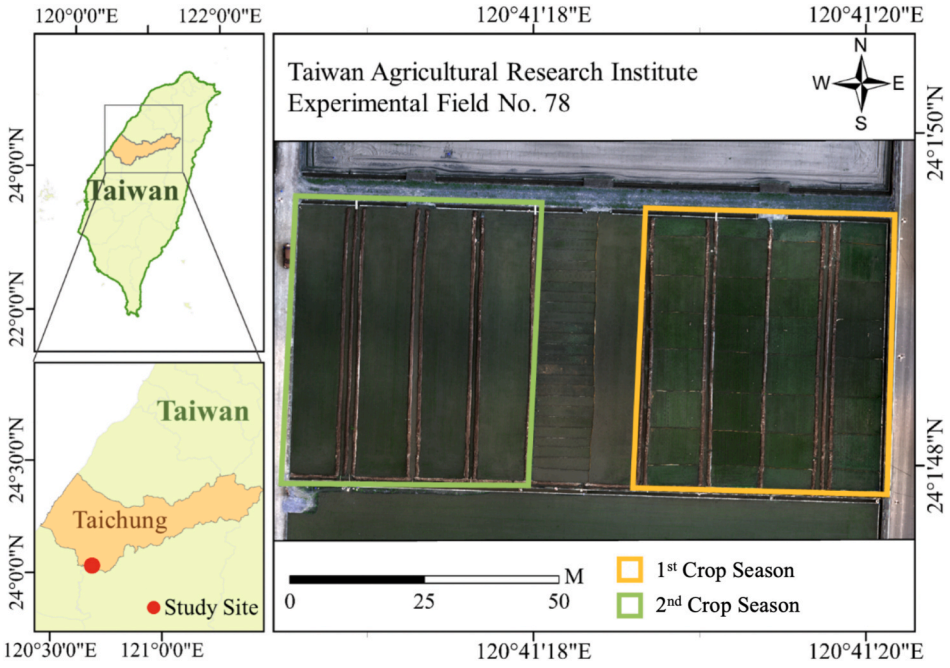

Fig. 2. Geographic location of the experimental site in Taichung city, Taiwan. The study site is marked on the Taiwan map (left), while the aerial image (right) shows the division of rice fields for the 1st (yellow) and 2nd (green) crop seasons. UAV-based multispectral imagery was collected over these plots during the 2020 and 2021 crop seasons.

methods, such as removing noncrop pixels from the collected images, were applied. This integration of advanced UAV sensing and image preprocessing provides a scalable and effective nitrogen management method for the precise farming of rice.

Typical image processing methods for pixel segmentation include spectral thresholding and ML-based classification. Yang et al. (2021) enhanced model accuracy by integrating multispectral imagery with ML to distinguish potato pixels from background pixels. Among unsupervised methods, the Otsu algorithm (Otsu, 1975) has been proven to be effective for simple background segmentation (Khan & Narvekar, 2022). Qiao et al. (2020) combined wavelet transformation with the Otsu algorithm for near-infrared image segmentation, and Dutta et al. (2022) used the Excess Green minus Excess Red index (ExGR) with the Otsu algorithm to successfully separate plants from the background. Regarding ML applications, Yang et al. (2015) employed the hue–saturation–value (HSV) color space and decision tree classification (DTC) to segment crop pixels from background elements in corn images. Yang et al. (2017) also applied DTC for land use classification in reservoir catchments; they addressed challenges related to spectral mixing. Li et al. (2014) revealed that soil background reduced the accuracy of nitrogen content predictions in corn when using the Normalized Difference Red Edge (NDRE) index. Qiao et al. (2020) demonstrated that removing the soil background of images improved chlorophyll content monitoring. Applying the Excess Green Index (ExG) and Excess Red Index (ExR) can enhance the spectral contrast between plants and soil (Woebbecke et al., 1995; Meyer & Neto, 2008), and ExGR further strengthens this contrast (Yang et al., 2020). Accordingly, this study employed Otsu-based segmentation and DTC preprocessing to improve nitrogen classification accuracy; the study used both raw spectral data and transformed VIs to enhance the precision of rice pixel extraction.

Various VIs and geometric traits have been explored for nitrogen classification in crops. Canopy coverage (CC) is a critical indicator of nitrogen status because nitrogen application influences canopy expansion (Haboudane et al., 2002). The Green Normalized Difference Vegetation Index (GNDVI) can be used to monitor chlorophyll levels in rice (García Cárdenas et al., 2018), and the Modified Triangle Vegetation Index 2 (MTVI2) can effectively track the nitrogen content in corn (Bagheri et al., 2013). Both the NDRE index and Red Edge Ratio Vegetation Index (RERVI) can be used to monitor the nitrogen status in rice leaves (Li et al., 2018), and the NDVI can be used to measure overall chlorophyll levels. The Optimized Soil-Adjusted Vegetation Index (OSAVI) can be used to reduce soil background interference during the monitoring of crop chlorophyll content (Haboudane et al., 2002). Accordingly, this study combined CC and several VIs as input features for classifying N levels; the study leveraged the complementary spectral and geometric information from these features to enhance model performance.

To improve nitrogen classification accuracy, feature selection techniques were employed to retain only the most relevant predictors and to reduce computational complexity. The applied feature selection techniques were random forest (RF) importance, recursive feature elimination (RFE), and chi-square tests (Wang & Xie, 2014; Shao & Dai, 2018; Zou et al., 2019; Bantan et al., 2020; Shi et al., 2021; Wang et al., 2021; Sheng et al., 2022; Barzin et al., 2022). ML models incorporating multiple features typically provide superior predictions than do linear statistical models. Moghimi et al. (2020) used SVM, RF, MLP, eXtreme Gradient Boosting, and quadratic discriminant analysis models to classify N levels in grape UAV multispectral imagery; the SVM model had the best performance. Li et al. (2022) implemented an AutoML framework to optimize hyperspectral image analysis for crop nutrient assessment, improving adaptability across agricultural conditions.

This study integrated UAV multispectral imagery, feature selection, and ML to classify N levels in rice fields, thus enabling precise data-driven nitrogen management for improving fertilizer application in rice farming.

2. Materials and methods

The workflow of this study is presented in Fig. 1. Initially, UAV imagery was collected and preprocessed, including labeling and segmentation to extract specific rice plant pixels. The segmentation results were then assessed to identify the most suitable algorithm. Spectral information from the segmented images was then obtained, and rice spectral features, cumulative growing degree days (CGDD), CC, and VIs were

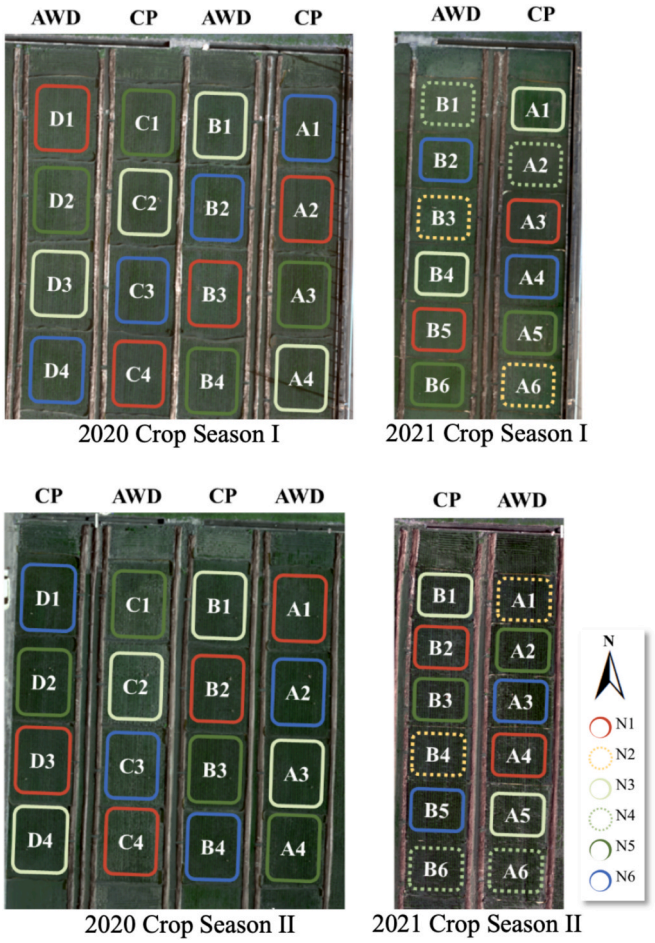

Fig. 3. Experimental field design during 2020 and 2021, showing six nitrogen treatments (N1–N6) in both the crop seasons I and II. The field following Conventional Planting (CP) and Alternate Wetting and Drying (AWD) irrigation methods. The field was divided into four sections (A, B, C, D), with individual plots labeled numerically. Four treatments (N1, N3, N5, N6) were selected for this research.

Table 1
N levels adopted for TNG71 cultivation. Three treatment categories—underfertilization, optimal, and overfertilization—correspond to the respective nitrogen applications (kg/ha).

N level	Categories	Nitrogen Fertilizer (kg/ha)
0	underfertilization	80 (N1)
1	optimal (lower bound)	120 (N3)
	optimal (upper bound)	160 (N5)
2	overfertilization	200 (N6)

Table 2
Specifications of UAV.

UAV name	DJI Matrice 210 RTK	Gryphon
UAV weight	4.4 kg (with 2 batteries) 5.2 kg (with 2 batteries)	8.5 kg (with a battery)
Max. flight load	6.14 kg	12.5 kg
Vertical precision	±0.1 m	±0.1 m
Horizontal precision	±0.1 m	±0.1 m
Crop season	2020 I, II & 2021 I	2021 II

calculated as inputs for N level classification models. The classification models were then trained and evaluated. This comprehensive approach enabled precise nitrogen assessments for rice cultivation, which could enhance the management of nitrogen fertilizer application.

Table 3
Flight mission parameters and multispectral sensor specifications, including altitude, overlap, resolution, spectral bands, and the estimated digitization footprint (GB/ha).

Parameter	MicaSense Altum
Flight height (m)	40
Front overlap (%)	80
Side overlap (%)	80
Flight speed (m/s)	< 2
Radiometric resolution (bits)	16
Spatial resolution (cm/pix)	1.77
Bands (nm)	Blue (475, 32)
(Center wavelength, bandwidth)	Green (560, 27)
	Red (668, 14)
	Red-edge (717, 12)
	NIR (842, 57)
Number of flight mission	26
Spatial coverage (ha)	0.5
Digitization footprint (GB/ha)	6.25

2.1. Data collection

The research site was at Experimental Field No. 78 of the Taiwan Agricultural Research Institute in Wufeng District, Taichung. UAVs equipped with multispectral sensors were used to capture images for the first and second (I and II) rice-growing seasons of 2020 and 2021; thus, four sets of images were obtained. The first growing season spanned from early March to early June, and the second season was from early August to early November. The growing periods for the first and second seasons were approximately 107 and 98 days, respectively. In both 2020 and 2021, the rice planting area was approximately 1300 m^2. In 2020, this area was divided into 16 plots of approximately 80 m^2 each; in 2021, it was divided into 24 plots of approximately 50 m^2 each. The areas are illustrated in Fig. 2. The rice was planted using transplantation with row and plant spacings of 0.3 and 0.21 m, respectively.

The TNG71 rice variety was selected because it is commonly grown in central Taiwan. Field management was performed with two irrigation methods: conventional planting (CP) and alternative wetting and drying (AWD) (Li et al., 2021). In CP, a water level of 3–5 cm is maintained. In AWD, irrigation is performed until the water reaches 3–5 cm but then ceases until the water level reaches 0 cm; irrigation is then resumed after 24 h until the water again reaches 3–5 cm. In 2020, TNG71 was fertilized at four N levels: N1 (80 kg/ha); N3 (120 kg/ha); N5 (160 kg/ha), and N6 (200 kg/ha). In 2021, two additional N levels (six total) were used: N2 (100 kg/ha) and N4 (140 kg/ha). For each nitrogen treatment, four replicates were conducted in 2020, and two replicates were conducted in 2021 (Fig. 3). N level classification was performed using data collected for the four levels (N1, N3, N5, and N6) in 2020 and 2021 during crop season I. N1, N3, N5, and N6 represent underfertilization, lower optimal, upper optimal, and overfertilization, respectively (Table 1). For detailed climate and soil data of the experimental field, please refer to Table A1 and Fig. A1.

For data collection, UAVs equipped with multispectral sensors were used. In 2020 and crop season I of 2021, a Matrice 210 RTK UAV from DJI (Shenzhen, China) was used. For crop season II of 2021, a Gryphon UAV from Avilon Intelligence (Tainan, Taiwan) was deployed. Details regarding these UAVs are listed in Table 2. All UAVs carried a MicaSense Altum multispectral sensor (AgEagle Aerial Systems, Lausanne, Switzerland). The flight parameters and sensor wavelengths are listed in Table 3, including the digitization footprint, which indicates data volume per ha (Marinello et al., 2019).

To ensure geometric accuracy, four ground control points were used to frame the study area. All UAV's data using a real-time kinematic satellite positioning instrument (SouthGNSS, Guangzhou, China), and base station coordinates were provided by the Taiwan Ministry of the

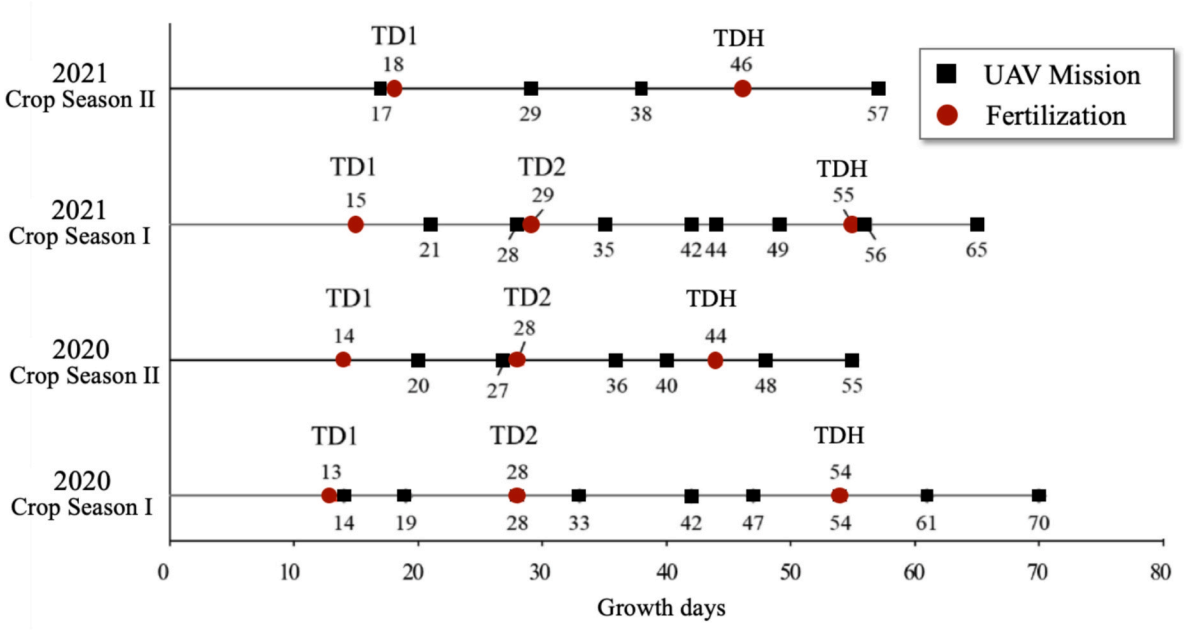

Fig. 4. Timeline of fertilization events (red circles) and UAV imaging missions (black squares) during the 2020 and 2021 crop seasons. UAV missions were conducted about bi-weekly, with rice pixel segmentation using data from TD1 to TDH and N level classification from TD2 to TDH in crop season I.

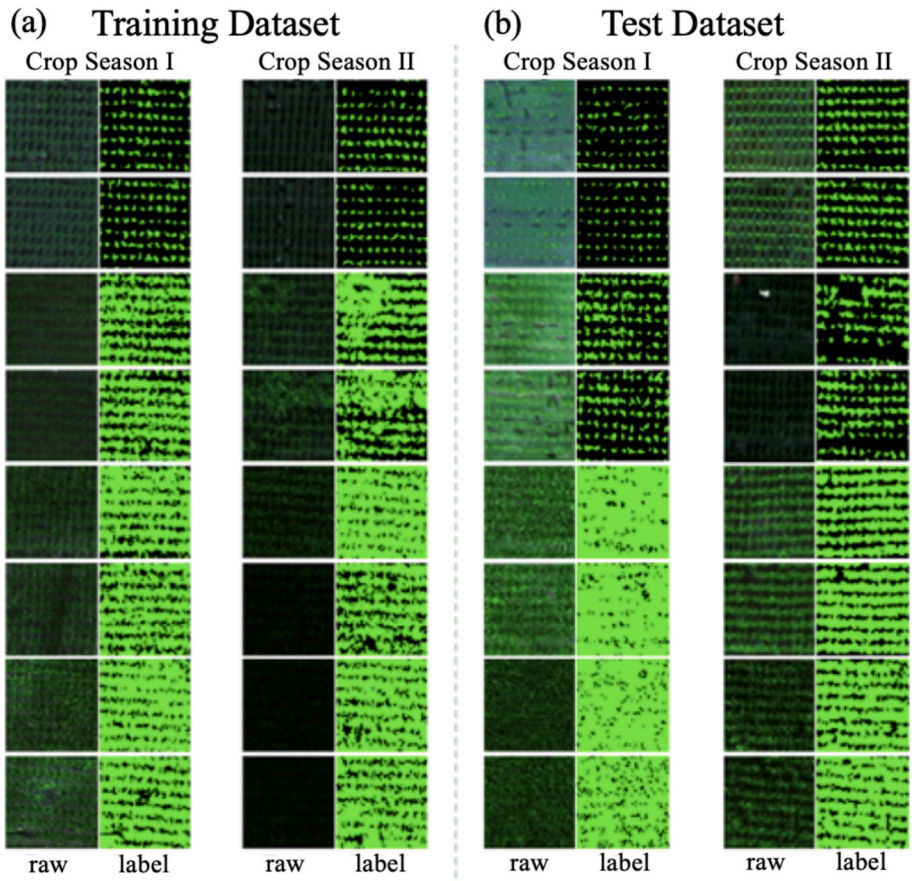

Fig. 5. Representative 128 × 128 image tiles and their ground-truth labels for rice pixel segmentation. (a) Training dataset samples from the 2020 Crop Seasons I and II. (b) Test dataset samples from the 2021 Crop Seasons I and II. Ground truth segmentation was manually annotated by domain experts, classifying pixels into rice plants and soil background.

Table 4
Specifications of the N level dataset used for classification. UAV images were collected from TD2 to TDH during the 2020 and 2021 crop seasons I, divided into Period I (TD2–TDH) and Period II (post-TDH). Data was split into training (80 %) and test (20 %) sets. Crop Season II was excluded due to different fertilization schedules.

Period	Cultivation stage	2020	2021	Training data	Test data
		Crop season I			
I	TD2-TDH	4 mission	4 mission	76	38
II	post-TDH	2 mission	2 mission	20	10

Table 5
The formula for HSV color space transformation.

Color Space		Formula	Source
HSV	Hue	$H = \begin{cases} \theta & if\ B' \le G' \\ 360^{\circ} - \theta & if\ B' > G' \end{cases}$	Smith, 1978
		$\theta = cos^{-1}\left\{ \frac{\frac{1}{2}[(R'-G')+(R'-B')]}{\sqrt{(R'-G')^2+(R'-B')(G'-B')}} \right\}$	
	Saturation	$S = 1 - \frac{3}{R'+G'+B'} min(R', G', B')$	
	Value	$V = \frac{1}{3}(R'+G'+B')$	

Table 6
VIs formula of rice pixel extraction.

Vegetation Index	Formula	Source
ExG (Excess Green Index)	$\frac{2\times G' - R' - B'}{B'+G'+R'}$	Woebbecke et al., 1995
ExR (Excess Red Vegetative Index)	$\frac{1.4\times R' - G'}{B'+G'+R'}$	Meyer & Neto, 2008
ExGR (The ExG minus ExR Vegetation Index)	ExG −ExR	Meyer & Neto, 2008

Interior's National Land Surveying and Mapping Center, ensuring a positional measurement error of less than ±1 cm. Flight missions were executed at an altitude of 40 m, and longitudinal and lateral image overlaps were set to 80 % to optimize photogrammetric processing and image stitching accuracy. The UAV operated at a flight speed of less than 2 m/s to maintain high image resolution and minimize motion blur. To reduce the number of flights turns and improve efficiency, the flight path was planned in the east–west direction along the long axis of the field, ensuring forward-facing flight during data collection and minimizing unnecessary maneuvering.

In addition to geometric corrections, spectral calibration was performed to enhance the reliability of the reflectance data. Before and after each flight, radiometric calibration was conducted using a calibrated reflectance panel to ensure consistency across all spectral bands. Multispectral data were processed using the standard workflow for the MicaSense Altum in Metashape (Agisoft LLC, Russia). This processing procedure included several key correction steps. First, panel detection and reflectance calibration were performed in accordance with the certified albedo values of the calibration panel. To minimize distortions caused by lens vignetting, a polynomial-based correction algorithm was implemented. Because variations in sunlight can influence reflectance readings, a downwelling light sensor was used to normalize radiance measurements, thus ensuring consistency under changes in solar conditions throughout the flight.

After radiometric and geometric corrections, orthomosaic processing was conducted in Metashape by performing image alignment, point cloud reconstruction, and digital surface model generation. The final orthomosaic image had a ground resolution of 6.36 mm per pixel; the reprojection error was 0.391 pixels, and the total root mean square error was 0.98 cm, ensuring high geometric fidelity. These corrections established a robust foundation for the subsequent analysis of N levels in rice fields by providing accurate and spatially consistent multispectral imagery.

The UAV missions were executed about biweekly to capture key phenological stages of rice growth and variations in nitrogen uptake. Rice image pixel segmentation was performed for data from the first topdressing (TD1) to the topdressing for head sprouting (TDH). N level classification was performed for images captured from the second topdressing (TD2) to TDH during crop season I in 2020 and 2021. UAV multispectral images were captured nine times in 2020 crop season I, eight times in 2021 crop season I, six times in 2020 crop season II, and four times in 2021 crop season II. The timeline of fertilization and number of images collected in each mission are detailed in Fig. 4.

To ensure accurate nitrogen classification, the collected dataset was divided into two periods: Period I (TD2–TDH) and Period II (post-TDH). This division was based on the physiological development of rice and its nitrogen uptake dynamics. Period I correspond to the critical vegetative and early reproductive growth stages, during which nitrogen demand is high and the canopy reflectance spectra varies considerably owing to changes in chlorophyll content and biomass accumulation. Period II occurs after TDH in the grain-filling stage when nitrogen redistribution dominates; canopy spectral changes stabilize in this phase.

In the rice pixel segmentation process, images were divided within defined grids into 128 × 128 pixel tiles. To prepare ground-truth data, domain experts used GIMP software to manually segment the images into two categories: rice plants and the soil background. Images from the 2020 crop seasons I and II were used as the training dataset, which comprised 737,280 data items (image tiles). Images from the 2021 crop seasons I and II were used as the test dataset, which contained 360,448 data items (Fig. 5). The dataset for N levels comprised images of the rice fields captured from TD2 to TDH during crop season I in 2020 and 2021. Images from crop season II were excluded because of differences in fertilization schedules between this season and the other season. This dataset was divided into two periods: TD2 to TDH (Period I) and post-TDH (Period II). In 2020, each of the four N levels was replicated in four separate plots, resulting in a total of 16 plots; in 2021, each level was replicated in two plots, resulting in a total of eight plots. For both years, data were captured four times for Period I and two times for Period II, resulting in 96 data items for Period I and 48 data items for Period II. These were divided into training and test datasets at a ratio of 80 %–20 %, as detailed in Table 4. This segmentation strategy enhanced the model's ability to generalize across different nitrogen application conditions.

2.2. Feature enhancement

For accurate N level monitoring, nonrice pixels must be eliminated. The rice image segmentation process was performed by using several raw spectral bands, namely blue (B), green (G), red (R), RE, and near infrared (NIR), in addition to the hue of HSV and three VIs (ExG, ExR, and ExGR). After normalizing the raw bands (Riehle et al., 2020), the hue and VIs were computed using the formulas in Tables 5 and 6. Each raw spectral band was normalized using min–max normalization at a 16-bit radiometric resolution, as described in Eqs. (1)–(5). The resulting normalized values are denoted by a prime symbol (e.g., B′).

$$B' = \frac{B - B_{min}}{B_{max} - B_{min}} \quad (1)$$

$$G' = \frac{G - G_{min}}{G_{max} - G_{min}} \quad (2)$$

$$R' = \frac{R - R_{min}}{R_{max} - R_{min}} \quad (3)$$

Table 7
VIs formula of N level classification.

Vegetation Index	Formula	Descriptive ability	Source
GNDVI (Green Normalized Difference Vegetation Index)	$\frac{NIR' - G'}{NIR' + G'}$	Chlorophyll concentration	Gitelson et al., 1996
MTVI2 (Modified Triangle Vegetation Index 2)	$\frac{1.8(NIR' - G') - 3.75(R' - G')}{\sqrt{(2NIR'+1)^2 - (6NIR' - 5\sqrt{R'}) - 0.5}}$	Leaf nitrogen status	Haboudane et al., 2004
NDRE (Normalized Difference Red Edge)	$\frac{NIR' - RE'}{NIR' + RE'}$	Leaf nitrogen status, Chlorophyll concentration	Barnes et al., 2000
NDVI (Normalized Difference Vegetation Index)	$\frac{NIR' - R'}{NIR' + R'}$	Leaf nitrogen status, Chlorophyll concentration	Rouse et al., 1973
OSAVI (Optimized Soil Adjusted Vegetation Index)	$\frac{1.16(NIR' - R')}{(NIR' + R' + 0.16)}$	Chlorophyll concentration	Lawrence & Ripple, 1998
RERVI (Red Edge Ratio Vegetation Index)	$\frac{NIR'}{RE'}$	Leaf nitrogen status	Tucker, 1979

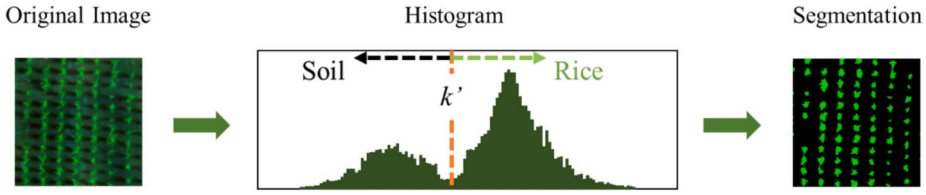

Fig. 6. Otsu algorithm for rice and soil pixels segmentation.

$$RE' = \frac{RE - RE_{min}}{RE_{max} - RE_{min}} \tag{4}$$

$$NIR' = \frac{NIR - NIR_{min}}{NIR_{max} - NIR_{min}} \tag{5}$$

CC was defined the ratio of rice pixels to the total pixels of the sample area (Qiao et al., 2020) and was calculated using Eq. (6). In these calculations, B′, G′, R′, RE′, NIR′, hue, and six VIs (GNDVI, MTVI2, NDRE, NDVI, OSAVI, and RERVI) were used as features. Hue was normalized as NHue by setting the maximum value to 360 and the minimum to 0, as indicated in Eq. (7). RERVI was normalized (NRERVI) by assuming a maximum RERVI value of 10, as expressed in Eq. (8). The VIs for N level classification are detailed in Table 7.

$$\mathrm{CC} = \frac{Area_{rice}}{Area_{all}} \tag{6}$$

$$\mathrm{NHue} = \frac{HSV\_H - HSV\_H_{min}}{HSV\_H_{max} - HSV\_H_{min}} \tag{7}$$

$$\mathrm{NRERVI} = \frac{RERVI - RERVI_{min}}{RERVI_{max} - RERVI_{min}} \tag{8}$$

CGDD is a frequently used indicator for assessing vegetation growth stages in rice cultivation. Sharma et al. (2021) established a relationship between cotton growth stages and CGDD, observing that growth speeds up with rising temperatures. CGDD is calculated by first determining growing degree days, as presented in Eqs. (9) and (10), where T_{max} is the daily maximum temperature and T_{min} is the daily minimum temperature; the base temperature for rice growth in Taiwan is 10 °C. In the formula for CGDD, n is the number of days of rice growth. In this study, temperature data (Fig. A1) were sourced from the Central Weather Bureau of Taiwan's Ministry of Transportation.

$$GDD = max\left[0, \left(\frac{T_{max} + T_{min}}{2} - T_b\right)\right] \tag{9}$$

$$CGDD = \sum_{i=1}^{n} GDD_i \tag{10}$$

2.3. Image processing

2.3.1. Rice pixel segmentation

Otsu introduced an algorithm for determining the optimal threshold k' for segmenting grayscale images into a binary form to differentiate target and background pixels. In this algorithm, pixels with values greater than k' are set to 1, and other pixels are set to 0; this process is illustrated in Fig. 6 and expressed in Eq. (11). The algorithm seeks to maximize the between-class variance ${\sigma_B}^2$ by evaluating it at various thresholds from 0 to $L - 1$, where L is the highest intensity value. The optimal threshold k' maximizes this variance, as expressed in Eqs. (12) and (13). The groups C_0 and C_1 comprise pixels with intensities greater than and less than k, respectively. The mean intensity values for these groups are μ_0 and μ_1, respectively, and P_0 and P_1 are the corresponding probabilities of pixel distribution for C_0 and C_1. This algorithm provides a robust framework for analyzing image pixel distribution and enhancing image segmentation fidelity.

$$g(x,y) = \begin{cases} 1, & f(x,y) > k' \\ 0, & f(x,y) \leqslant k' \end{cases}, \quad \begin{matrix} x = 0,1,\ldots,N-1 \\ y = 0,1,\ldots,M-1 \end{matrix} \tag{11}$$

$${\sigma_B}^2(k) = P_0(\mu_0 - \mu_t)^2 + P_1(\mu_1 - \mu_t)^2 \tag{12}$$

$${\sigma_B}^2(k') = \max_{0 \leq k \leq (L-1)} {\sigma_B}^2(k) \tag{13}$$

The Classification and Regression Tree method builds DTs by repeatedly splitting a parent node into two child nodes to either maximize information gain or decrease Gini impurity. The process continues until a stopping criterion is reached or further splitting does not improve the model. Information gain is calculated as the entropy values [defined in Eq. (14)] before and after the split; maximizing the entropy results in the optimal split, as indicated in Eq. (15). Similarly, the Gini impurity is calculated as expressed in Eq. (16) and is optimized as indicated in Eq. (17). Eq. (14) presents the formula for $\Delta I(t)$, which represents the information gain for a split t. Here, $I(t)$ is the initial entropy, and P_{left} and P_{right} are the proportions of data points in the left and right child nodes, respectively, after a split. In Eq. (15), T is the threshold that maximizes $\Delta I(t)$. For the Gini index in Eq. (16), $e(t)$ indicates the expected classification error; in Eq. (17), $i(t)$ denotes the impurity calculated from the probability $p(i)$ for class i in the dataset. These equations help fine-tune

Table 8
Hyperparameter search space for the Decision Tree Classifier (DTC) used in this study. A grid search with 10-fold cross-validation was conducted to determine the optimal settings for splitting criteria, tree depth, and minimum samples required for node splitting. The class weight was set to balanced to address class imbalance.

Properties	Hyperparameter
Confounding value	entropy, gini
Max. depth	1, 5, 10, 15, 20, 25, 30, 35, 40, 45, 50, 55, 60, 65, 70, 75, 80, 85, 90, 95, 100
Min. samples split	2, 50, 100, 150, 200, 250, 300, 350, 400, 450, 500, 550, 600, 650, 700, 750, 800, 850, 900, 950, 1000, 1050, 1100, 1150, 1200
Class weight	balanced

Table 9
Hyperparameter search space for the Support Vector Machine (SVM) model used in this study. The model employs a Radial Basis Function (RBF) kernel, with penalty parameter C and kernel coefficient γ selected from a wide range through grid search and 10-fold cross-validation. The class weight is set to balanced to handle class imbalances, and the one-vs-rest (OvR) decision function is used for multi-class classification.

Properties	Hyperparameter
Kernel	Radial Basis Function (RBF)
Penalty Parameter C	10^{-5}, 10^{-4}, 10^{-3}, 10^{-2}, 10^{-1}, 10^{0}, 10^{1}, 10^{2}, 10^{3}, 10^{4}, 10^{5}
γ	10^{-5}, 10^{-4}, 10^{-3}, 10^{-2}, 10^{-1}, 10^{0}, 10^{1}, 10^{2}, 10^{3}, 10^{4}, 10^{5}
Class Weight	Balanced
Decision Function Shape	One-vs-rest (OvR)

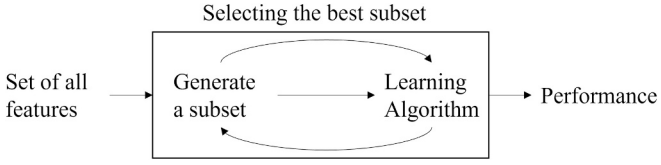

Fig. 7. RFE feature selection process.

the DT for the most effective classification results.

$$\Delta I(t) = I(t_p) - [P_{left} \times I(t_{left}) + P_{right} \times I(t_{right})] \tag{14}$$

$$\mathrm{T} = \mathrm{argmax}[\Delta I(t)] \tag{15}$$

$$e(t) = -\sum_{i=1}^{c} p(i) log_2 p(i) \tag{16}$$

$$i(t) = \sum_{i=1}^{c} p(i) \times (1 - p(i)) \tag{17}$$

CART implemented in scikit-learn chooses the best split based on criteria such as Gini or entropy. The model adjusts to different training datasets by evaluating various hyperparameters, as shown in Table 8, and hyperparameters detailed below.

2.3.2. N level classification

The *k* nearest neighbor (KNN) algorithm classifies data points by their proximity in a feature space. The distances between points can be calculated using various metrics to determine the "neighborhood" of each data point. The choice of distance metric substantially affects the performance of the KNN algorithm. Commonly used metrics include the Euclidean, Manhattan, and Minkowski distances, as indicated in Eqs. (18)–(20). The Minkowski distance is equivalent to the Euclidean distance for $p = 2$. (Raschka & Mirjalili, 2019; Imandoust & Bolandraftar, 2013).

$$\mathrm{D} = \sqrt{\sum_{i=1}^{n} (x_i - y_i)^2} \tag{18}$$

$$\mathrm{D} = \sum_{i=1}^{n} |x_i - y_i| \tag{19}$$

$$\mathrm{D} = \left(\sum_{i=1}^{n} |x_i - y_i|^p \right)^{\frac{1}{p}} \tag{20}$$

The SVM model is a robust classification algorithm. It constructs a hyperplane in a high-dimensional space, and this hyperplane separates data points into categories such that the distance between the data points and the hyperplane is maximized. The hyperplane is described in Eq. (21), where *w* represents the weight vector and *b* represents the bias. The data points closest to the hyperplane are called support vectors and affect the plane's position and orientation. The SVM model uses kernel functions to handle nonlinear relationships between data points. This kernel function is represented in Eq. (22). It transforms the data into a higher-dimensional space to facilitate separation by the hyperplane. In this study, several hyperparameters, including the kernel type (e.g., radial basis function), penalty parameter, and kernel coefficient γ, which considerably affect model performance, were obtained through 10-fold cross-validation. The hyperparameter search spaces are listed in Table 9.

$$w^T x + b = 0 \tag{21}$$

$$\mathrm{K}(X_i, X_j) = \phi(X_i)^T \phi(X_j) = e^{\left(-\frac{\|X_i - X_j\|^2}{2\sigma^2}\right)} = e^{(-\gamma \|X_i - X_j\|^2)}, \gamma > 0 \tag{22}$$

During feature selection, the potential influence of each feature variable on the prediction target must be considered. The RF importance method ranks features by their contribution to a binary classification model and provides a basis for feature selection. Furthermore, the RFE process iteratively removes the least relevant features during multivariate regression to identify essential features. The order of feature selection in RFE serves as a reference for feature ranking. Finally, a chi-square test was also used to assess the significance of feature distributions for different nitrogen fertilizer categories in order to determine the relevance of each feature in classification.

The RF importance algorithm evaluates the reduction in impurity at each DT node according to the Gini impurity or entropy. Features that reduce impurity more are assigned higher importance (Lowe & Kulkarni, 2015). The Gini impurity for dataset *D* is calculated as shown in Eq. (23), where p_i represents the proportion of class *i* in *D* (Cassidy & Deviney, 2014; Yuan et al., 2021). The reduction in Gini impurity after a split by a feature *k* is calculated using Eq. (24), where $D_{incoming}$ represents the incoming dataset and P_L and P_R represent the proportions of the dataset at the left and right child nodes after the split, respectively. Features with a greater Gini impurity reduction are assigned a greater importance in RF; the average impurity reduction of a feature across trees is its final importance score.

$$I(D) = 1 - \sum_{i=1}^{n} (p_i)^2 \tag{23}$$

$$\Delta I(D_{incoming}, k) = I(D_{incoming}) - P_L \bullet I(D_L) - P_R \bullet I(D_R) \tag{24}$$

RFE is a wrapper method for feature selection that iteratively removes irrelevant or harmful features by evaluating an estimation model's calculated feature weights or relevance (Lin et al., 2012; Darst et al., 2018; Misra & Yadav, 2020). The goal is to identify the most relevant features of the model. An overview of the RFE process is illustrated in Fig. 7.

Table 10
Performance of the Otsu model using different spectral and color-transformed features. Among spectral bands, NIR' achieves the highest overall accuracy (OA), while ExG outperforms other color transformations with 79.4 % OA and the highest rice recall (77.6 %).

Method	Feature	Class Soil (%)			Class Rice (%)			OA (%)
		Precision	Recall	F1-Score	Precision	Recall	F1-Score	
Otsu	B′	45.4	76.7	57.1	67.6	34.6	45.7	52.1
	G′	55.5	78.7	65.1	78.5	55.1	64.7	64.9
	R′	46.9	39.7	43.0	61.4	68.0	64.5	56.3
	RE′	59.9	87.2	71.1	86.6	58.5	69.9	70.5
	NIR′	64.6	98.6	78.1	98.4	61.6	75.8	77.0
	NHue	45.1	53.2	48.8	61.8	53.9	57.6	53.6
	ExG	72.2	82.1	76.8	85.9	77.6	81.5	79.4
	ExR	71.0	87.0	78.2	89.0	74.8	81.3	79.9
	ExGR	71.9	84.0	77.5	87.1	76.7	81.5	79.7

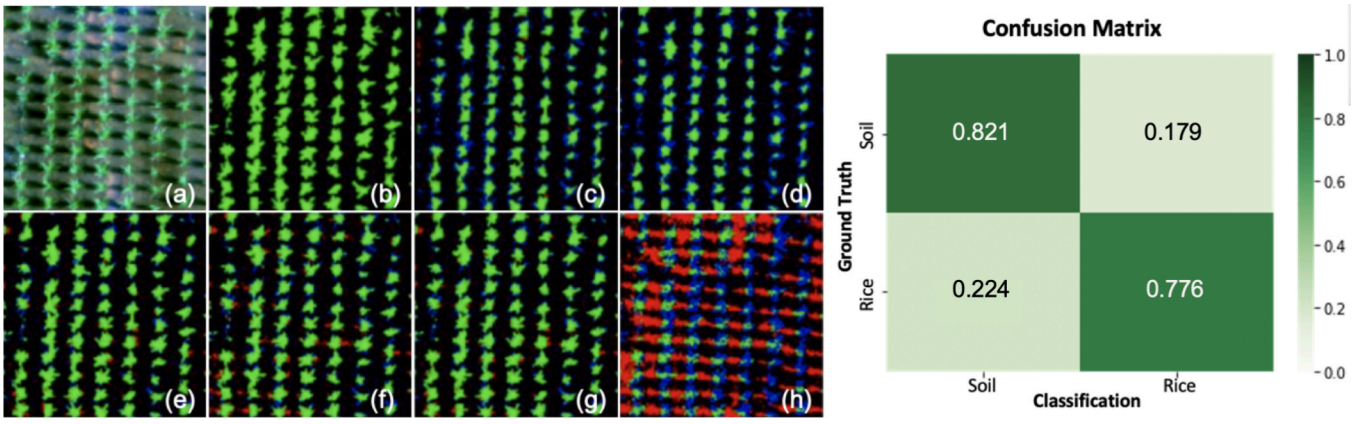

Fig. 8. Otsu-based segmentation results using various features. Left: (a)visible light, (b)ground truth, (c)RE', (d)NIR', (e)ExG, (f)ExR, (g)ExGR, and (h)NHue. Blue and red regions denote Type I and Type II errors, respectively. Right: confusion matrix of ExG.

Table 11
Performance of the Decision Tree Classifier (DTC) using different spectral and color-transformed features. Among raw spectral bands, NIR' achieves the highest performance with an F1-score of 90.2 % and an OA of 89.0 %. The composite feature model "all" further improves performance, achieving the highest rice recall (95.3 %), F1-score (90.8 %), and OA (88.8 %), making it the most effective approach for rice pixel segmentation.

Method	Feature	Class Soil (%)			Class Rice (%)			OA (%)
		Precision	Recall	F1-score	Precision	Recall	F1-score	
DTC	B′	81.1	37.2	51.0	67.8	93.8	78.7	70.3
	G′	61.8	19.2	29.3	61.4	91.6	73.5	61.5
	R′	83.7	36.3	50.6	67.7	95.0	79.0	70.6
	RE′	60.3	50.8	55.1	68.5	76.3	72.2	65.7
	NIR′	82.8	92.7	87.5	94.3	86.4	90.2	**89.0**
	NHue	84.7	63.1	72.3	77.8	91.9	84.2	79.9
	ExG	96.6	54.2	69.4	75.2	98.7	85.3	80.2
	ExR	95.8	55.7	70.4	75.7	98.3	85.5	80.6
	ExGR	96.6	53.3	68.7	74.8	98.6	85.1	79.8
	All	92.3	79.7	85.5	86.8	**95.4**	**90.8**	**88.8**

Feature selection aims to remove less-significant features for classification. A chi-square test was also employed to assess the independence between two data distributions. Higher chi-square values indicate that two variables are less likely to be independent. Conversely, lower values indicate independence. These chi-square values can be used to select appropriate features. The chi-square test is a filter method for feature selection (Saeys et al., 2007), and it is expressed in Eq. (25), where A denotes the observed values and E denotes the expected values.

$$x^2 = \sum \frac{(A-E)^2}{E} \tag{25}$$

2.3.3. Performance estimation

A confusion matrix was employed to measure key metrics for evaluating the accuracy of the classification models, such as precision, recall, F1 score, and overall accuracy (OA). Precision is the proportion of correct predictions for a class relative to all predictions made and is defined in Eq. (26). A higher precision level indicates fewer false positives. Recall, defined in Eq. (27), is the proportion of correct predictions for a class relative to all actual instances of that class. A higher recall level signifies fewer false negatives. The F1 score combines precision and recall [Eq. (28)] and provides a balanced measure of a model's accuracy. Scores closer to 1 indicate better performance; low scores suggest that a model struggles to predict certain classes. The OA, calculated through Eq. (29), measures the number of correct classifications across all categories as the ratio of correct predictions to the total number of data points. These metrics provide a comprehensive evaluation of a model's inference capabilities, enabling a detailed assessment of both per-class and overall performance.

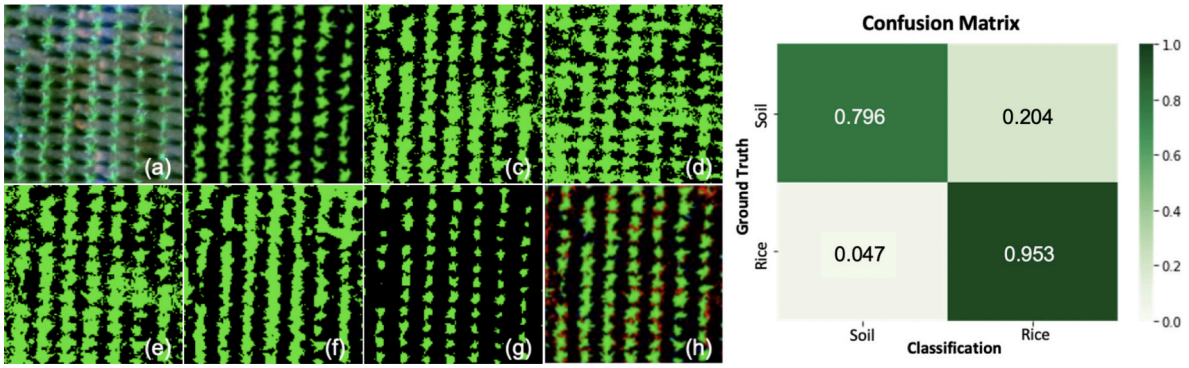

Fig. 9. DTC classification result visualization. Left: (a)visible light, (b)ground truth, (c)ExG, (d)ExR, (e)ExGR, (f)RE', (g)NIR', and (h) the "All" feature combination. Right: confusion matrix of ExG.

Table 12
Comparison of KNN and SVM performance for N Level classification using a 16-feature dataset. SVM outperforms KNN in Period I (60.0 % vs. 50.0 % OA), while both achieve 70.0 % OA in Period II. SVM performs better in Level 0 and Level 1 classifications, whereas KNN struggles with Level 2 in Period I but improves in Period II. These results highlight SVM's advantage in handling nonlinear classification.

N Level		Period I (%)		Period II (%)	
		KNN	SVM	KNN	SVM
Level 0	Precision	60.0	75.0	100	100
	Recall	100	100	50.0	100
	F1-score	75.0	85.7	66.7	100
Level 1	Precision	60.0	75.0	57.1	57.1
	Recall	50.0	50.0	100	100
	F1-score	54.5	60.0	72.7	72.7
Level 2	Precision	20.0	37.5	100	100
	Recall	20.0	60.0	50.0	25.0
	F1-score	20.0	46.2	66.7	40.0
	OA	50.0	60.0	70.0	70.0

$$Precision = \frac{The number of correct predictions for class n}{The number of all predictions for class n} \quad (26)$$

$$Recall = \frac{The number of correct predictions for class n}{The number of classes n} \quad (27)$$

$$F1 - score = \frac{2 \times Precision \times Recall}{Precision + Recall} \quad (28)$$

$$Overall Accuracy = \frac{The sum of the correct predictions for each category}{The number of data} \quad (29)$$

3. Results and Discussion

3.1. Rice pixels Segmemtation

3.1.1. Otsu model performance

In models that used features based on raw spectral bands, the RE′ and NIR′ features were associated with superior segmentation performance compared with the visible-band features (Table 10) owing to the higher reflectance intensity of these bands for chlorophyll. For the unsupervised Otsu algorithm, both soil recall and rice precision were high. NIR′ of soil category was associated with the highest recall (98.6 %), rice category precision (98.4 %), F1 score (75.8 %), and OA (77.0 %). Among the color space transformation features and VIs, ExG was associated with the highest recall, F1 score, and OA for rice classification (77.6 %, 81.5 %, and 79.4 %, respectively). Rice pixels are critical inputs for N level classification and CC calculations; thus, successfully identifying rice areas is crucial for a model, and rice recall is the key performance indicator. The results obtained for the Otsu algorithm are presented in Fig. 8; blue and red pixels represent Type I and Type II errors, respectively. Fig. 8(e) reveals that ExG outperformed NIR in terms of recall and OA; thus, it was the best feature for Otsu-based rice and soil segmentation.

Table 13
SVM classification performance using features selected by RF Importance. OA improved to 60.0 % (Period I) and 70.0 % (Period II) with grid search on selected features. Compared to using all features, the subset provided a more balanced classification, maintaining Level 0 precision in Period II while improving recall and F1-score for Level 2 despite a slight precision drop.

N Level	Number of features	Period I	Period II
		6	6
Level 0	Precision	40.0 %	100 %
	Recall	66.7 %	50.0 %
	F1-score	50.0 %	66.7 %
Level 1	Precision	80.0 %	60.0 %
	Recall	66.7 %	75.0 %
	F1-score	72.7 %	66.7 %
Level 2	Precision	40.0 %	75.0 %
	Recall	40.0 %	75.0 %
	F1-score	40.0 %	75.0 %
	OA	60.0 %	70.0 %

3.1.2. Decision tree model performance

The results for the DTC model are presented in Table 11. These results represent the best outcomes after hyperparameter tuning. For models using raw bands, precision and recall between soil and rice categories varied greatly for visible-light bands; this was likely due to data imbalance. Although rice recall was high for the visible bands, the precision level was generally lower, and many pixels were incorrectly classified as rice. The F1 score and OA, which consider the balance between precision and recall. Of the raw bands, NIR′ resulted in the best performance, with an F1 score of 90.2 % and an OA of 89.0 %. The optimal hyperparameters for the NIR′-based DTC model were the entropy criterion, a max depth of 5, and a minimum sample split of 2. For the color space transformation and VI features, precision and recall had discrepancies for both soil and rice categories; the corresponding F1 score was approximately 85 %, and the OA was approximately 80 %, indicating reliable performance that is comparable to that of the raw bands. The difference between the DTC model and Otsu algorithm is the DTC model's ability to incorporate composite features for training. The DTC model included nine combined features labeled "All." The optimal hyperparameters for training were the entropy criterion, a max depth of 15, and a minimum sample split of 150. These increases were due to the larger number of features.

Compared with models using individual features—raw bands, color space transformations, or VIs—the models using composite features

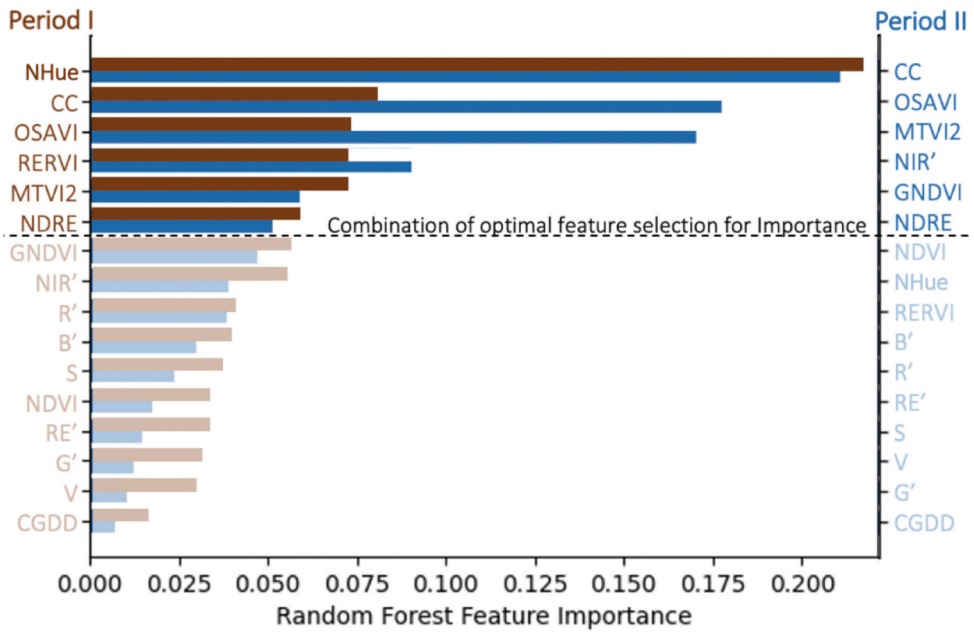

Fig. 10. Random Forest-based feature importance for Periods I and II. The optimal feature set was reduced from 16 to 6. Most selected features remained stable across periods, except for NHue and NIR'. Reducing the feature space improves inference stability across N levels, highlighting the significance of color transformation, coverage, and vegetation indices (VIs).

Table 14
SVM classification results using features selected by Recursive Feature Elimination (RFE). RFE-based feature selection improved OA to 75.0 % (Period I) and 80.0 % (Period II), outperforming models using all features or RF-selected features. The optimal feature set consisted of nine features in Period I and three in Period II, with RE' and NIR' consistently ranking among the top contributors, highlighting their importance in N Level classification.

N Level	Number of features	Period I	Period II
		9	3
Level 0	Precision	75.0 %	100 %
	Recall	100 %	50.0 %
	F1-score	85.7 %	66.7 %
Level 1	Precision	88.9 %	66.7 %
	Recall	66.7 %	100 %
	F1-score	76.2 %	80.0 %
Level 2	Precision	57.1 %	100 %
	Recall	80.0 %	75.0 %
	F1-score	66.7 %	85.7 %
	OA	75.0 %	80.0 %

Table 15
SVM classification results using features selected by the Chi-square test. The optimal feature subset (NDRE, GNDVI, RERVI, and CC) achieved an OA of 60.0 % (Period I) and 90.0 % (Period II), outperforming previous feature selection methods in Period II. The results suggest that these selected features effectively explain N level variations, particularly in the later growth stage.

N Level	Number of features	Period I	Period II
		4	4
Level 0	Precision	100 %	100 %
	Recall	50.0 %	100 %
	F1-score	66.7 %	100 %
Level 1	Precision	50.0 %	100 %
	Recall	75.0 %	75.0 %
	F1-score	60.0 %	85.7 %
Level 2	Precision	66.7 %	80.0 %
	Recall	50.0 %	100 %
	F1-score	57.1 %	88.9 %
	OA	60.0 %	90.0 %

exhibited superior performance in rice pixel segmentation, achieving a recall of 95.3 %, an F1 score of 90.8 %, and an OA of 88.8 %. The unsupervised Otsu algorithm efficiently classified the soil background and rice categories and yielded the best results with the ExG feature. However, the supervised DTC model trained on the composite features achieved higher precision. Compared with single-feature models, the composite-feature DTC model had fewer Type I and Type II errors, a higher F1 score, and a higher OA; thus, it is the recommended approach for rice pixel segmentation. With nine features as its input, the DTC model could successfully identify rice pixels for CC calculations, providing a feature for N level classification. Fig. 9 presents the DTC model results.

3.2. N level classification

A N level dataset was created to develop KNN and SVM models for classification. The classification results are summarized in Table 12. The SVM model outperformed the KNN model in Period I, achieving an OA of

Table 16
Dunn-Bonferroni analysis of feature significance by N level. Each feature's statistical significance is evaluated based on p-values ($p < 0.05$: *, $p < 0.01$: **, $p < 0.001$: ***). The most significant features ($p < 0.001$) across both periods include GNDVI, MTVI2, NDRE, NDVI, OSAVI, RERVI, and CC.

Feature	*p*-value		Feature	*p*-value	
	Period I	Period II		Period I	Period II
B′	0.053	0.000***	**GNDVI**	0.000***	0.000***
G′	0.007**	0.000***	**MTVI2**	0.000***	0.000***
R′	0.003**	0.000***	**NDRE**	0.000***	0.000***
RE′	0.097	0.002**	**NDVI**	0.000***	0.000***
NIR′	0.016*	0.000***	**OSAVI**	0.000***	0.000***
NHue	0.000***	0.000***	**RERVI**	0.000***	0.000***
S	0.035*	0.016*	**CC**	0.000***	0.000***
V	0.007**	0.000***			

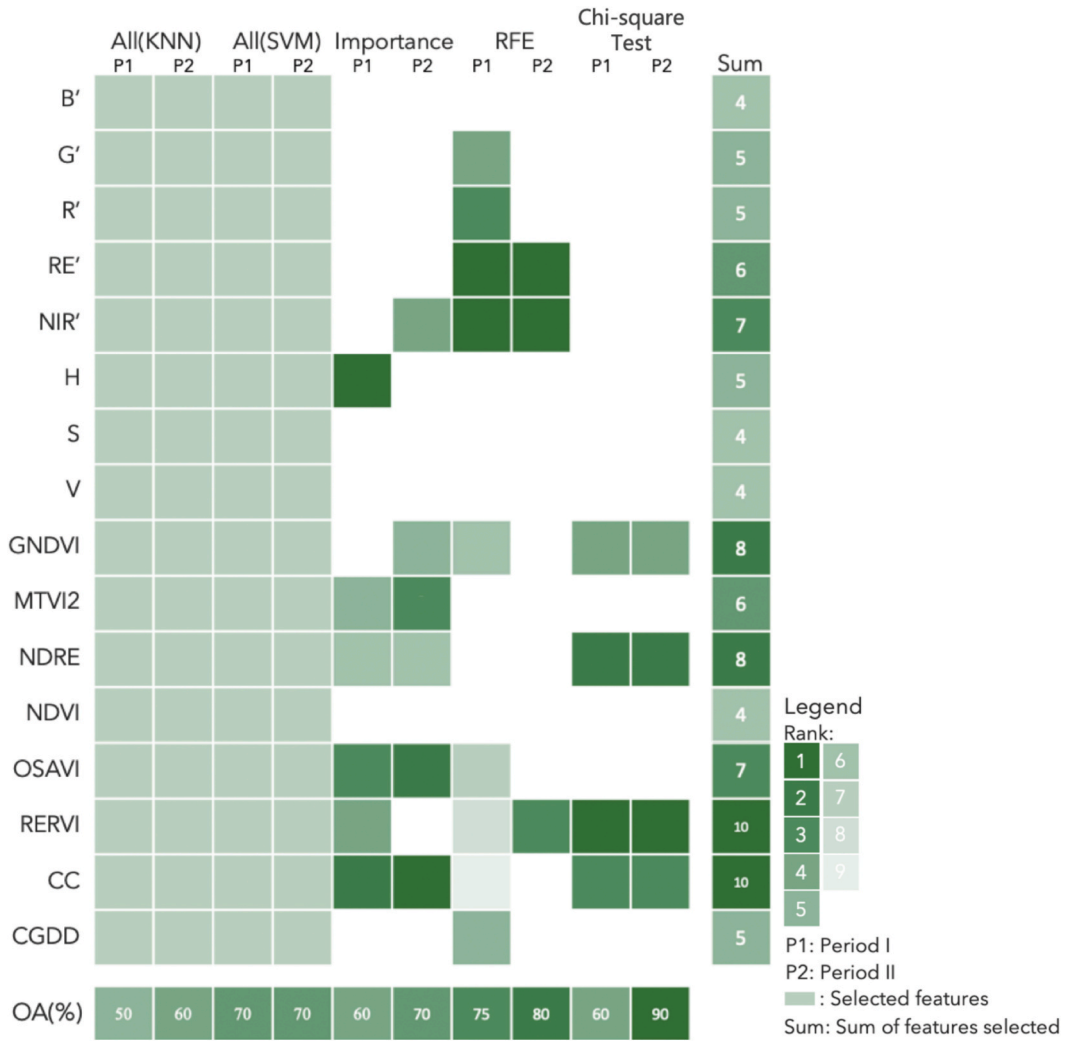

Fig. 11. Comprehensive feature selection outcomes for Periods I (P1) and II (P2) using KNN, SVM, RF Importance, RFE, and the Chi-square test. Selected features are marked in green, with darker shades indicating higher rankings. The rightmost column shows how often each feature was selected across methods. RERVI and CC were the most frequently chosen features, followed by GNDVI, NDRE, OSAVI, and NIR', demonstrating their strong influence on N level classification.

60.0 %, higher than the KNN model's 50.0 %. Both models exhibited improved performance in Period II, reaching an OA of 70.0 %. Because the KNN model relies on distance-based optimization for classification and the SVM model leverages hyperplane-based separation, the SVM model was more effective in handling the nonlinear relationships in N level classification.

Hyperparameter tuning significantly influenced model accuracy. For the KNN model, the best-performing distance metric was the Minkowski distance; its optimized hyperparameters included $p = 2$. The optimal *n_neighbors* setting (ranging from 1 or 7) depended on the feature selection approach. The SVM model achieved the highest classification accuracy using an RBF kernel, with C values ranging from 10^2 to 10^4 and γ values of either 0.1 or 1. It maintained a balanced class weight setting and adopted an OvR decision function, which simplifies multiclass problems by training a binary classifier for each class. A comparison of these models indicates that the SVM model, with its ability to optimize hyperplanes and leverage kernel-based transformations, provides a more robust framework for N level classification than the KNN model — particularly when feature selection methods are applied.

For N level classification performance in Period I and Period II, the precision, recall, and F1 score varied between the models, highlighting the complexity of nitrogen modeling. As shown in Table 12, the SVM model consistently outperformed the KNN model in Level 0 classification. In Level 1 classification, the SVM model had a slight advantage over the KNN model in Period I, and both models performed equally in Period II. In Level 2 classification, the KNN model exhibited poor performance in Period I but performed slightly better in Period II. The SVM model had better performance overall and was therefore optimized through feature selection methods.

In the RF importance method, a grid search was applied to evaluate combinations of features. The best results were used as input for the SVM model, and the results are listed in Table 13. The OA rates for Periods I and II were 60.0 % and 70.0 %, respectively. However, the use of the features selected by importance resulted in slightly better performance compared with the use of all features. Large differences in classification performance were observed between N levels. After feature selection, precision levels were consistent for Level 0 in Period II, but the recall and F1 score decreased notably. Conversely, in Level 2, the recall and F1 score were higher, but precision declined. These observations suggest that the selected feature combination resulted in more balanced inference performance across levels, particularly in Period II.

Fig. 10 displays the RF importance values of all features. The optimal feature set had six features. In Period I, the optimal features were NHue, CC, OSAVI, RERVI, MTVI2, and NDRE. In Period II, the top features were CC, OSAVI, MTVI2, NIR′, GNDVI, and NDRE. Thus, the feature set was reduced from 16 to 6, and the contributions were similar across periods for all selected features except for NHue and NIR′. Accordingly, half of the selected features, particularly the VIs, provided stable contributions

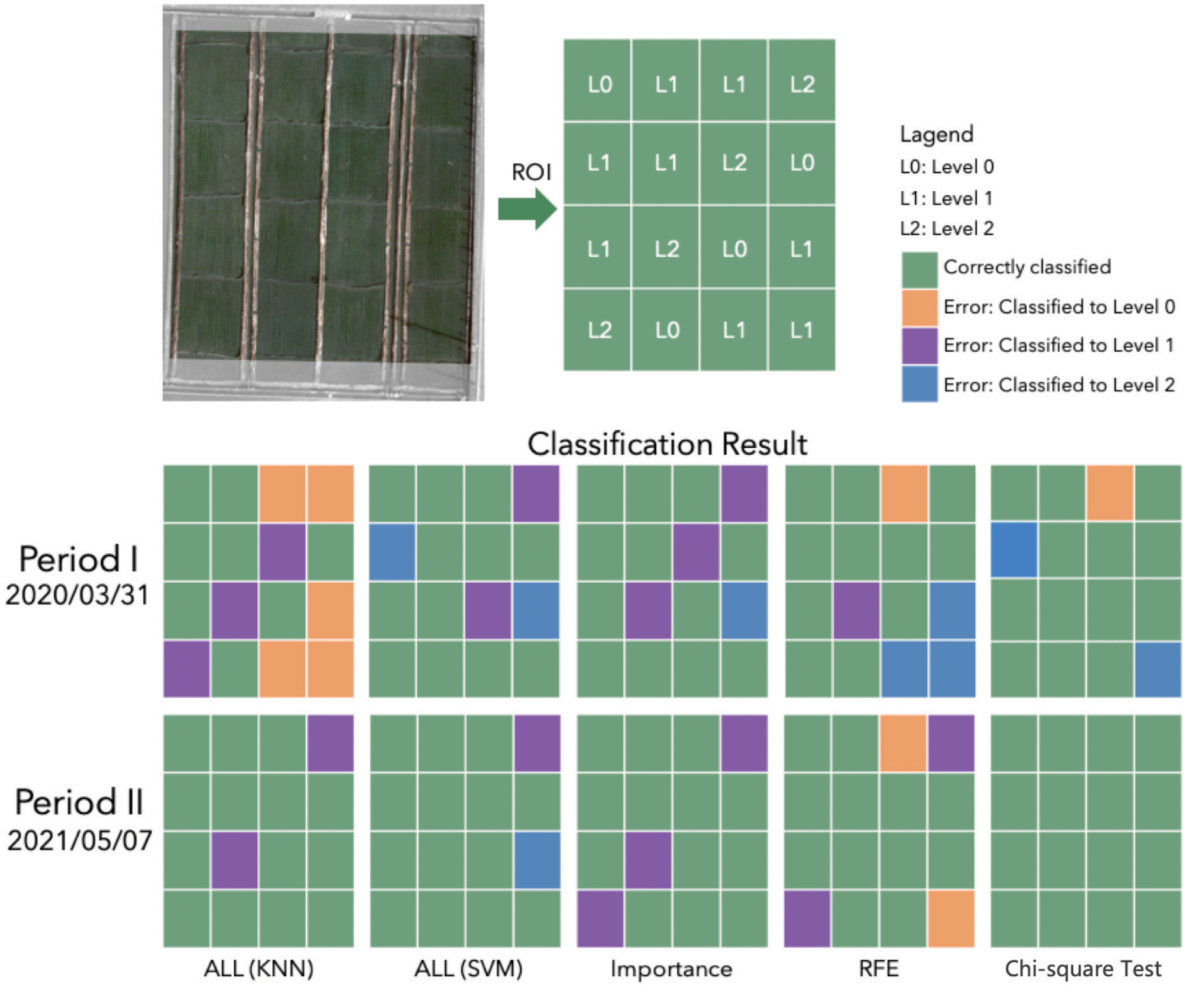

Fig. 12. Visualization results for each model and feature selection method. The map displays ROI and classification levels (L0, L1, L2). Correctly classified areas are shown in green, while errors are color-coded by misclassified levels. The grid compares performance across models (KNN, SVM) and feature selection methods (RF Importance, RFE, Chi-square test).

in both periods. NHue and CC, representing color space transformation and coverage, were the most important features, and CGDD had the lowest contribution. This was likely due to the lack of variation of CGDD between levels.

The relationships of features with N levels can vary in their correlation. Composite features were used to train the models. A multiple linear regression model can be used to fit an equation between features and N levels, and RFE can then select features based on their contribution, as indicated by the regression coefficients of the model. RFE adjusts the number of features iteratively and assesses the model's predictive performance at each step to determine the contribution of each feature. The test performance of the SVM model trained using the RFE-selected features is shown in Table 14.

The OA rates of the SVM model with RFE in Periods I and II were 75.0 % and 80.0 %, respectively, outperforming models that used all features or the RF importance features. The optimal feature set for Period I comprised nine features, which are expressed as follows (ranked by RFE): RE′, NIR′, R′, G′, CGDD, GNDVI, OSAVI, RERVI, and CC. The optimal feature set for Period II contained RE′, NIR′, and RERVI. RE′ and NIR′ were consistently the top contributors across both periods, indicating their strong correlation with N levels. For nitrogen Level 2, models using RFE features achieved better precision, recall, and F1 score values in both Periods I and II compared with models using all features or those selected by RF importance.

Feature significance indicates the explanatory capability of each feature for N levels. A chi-square test was used to assess the statistical significance of features in relation to N levels, and the features with the strongest relationships were selected for model training and testing. The test results are summarized in Table 15.

The OA of the SVM model that used features selected by the chi-square test was 60.0 % for Period I and 90.0 % for Period II. For both periods, the optimal feature set had four features: NDRE, GNDVI, RERVI, and CC. The OA and N level classification results obtained in Period II were superior to those obtained in Period I. The individual *p*-values of all features from the chi-square test are listed in Table 16, where $p < 0.05$ (marked as *) indicates significant, $p < 0.01$ (marked as **) indicates highly significant, and $p < 0.001$ (marked as ***) indicates extremely significant features. The best-performing feature set in both periods contained only extremely significant features. These results also reveal that most features had higher significance in Period II than in Period I.

Dunn–Bonferroni tests were conducted to further assess feature significance between levels. Level 0 and Level 2 had the greatest differences, and Level 1 and Level 2 had the smallest differences. This result highlights the difficulty of distinguishing between conventional and excessive fertilizer treatments by considering a single feature. These findings align with the observed classification performance; that is, precision, recall, and F1 score were more consistent for Levels 0 and 1 than for Level 2.

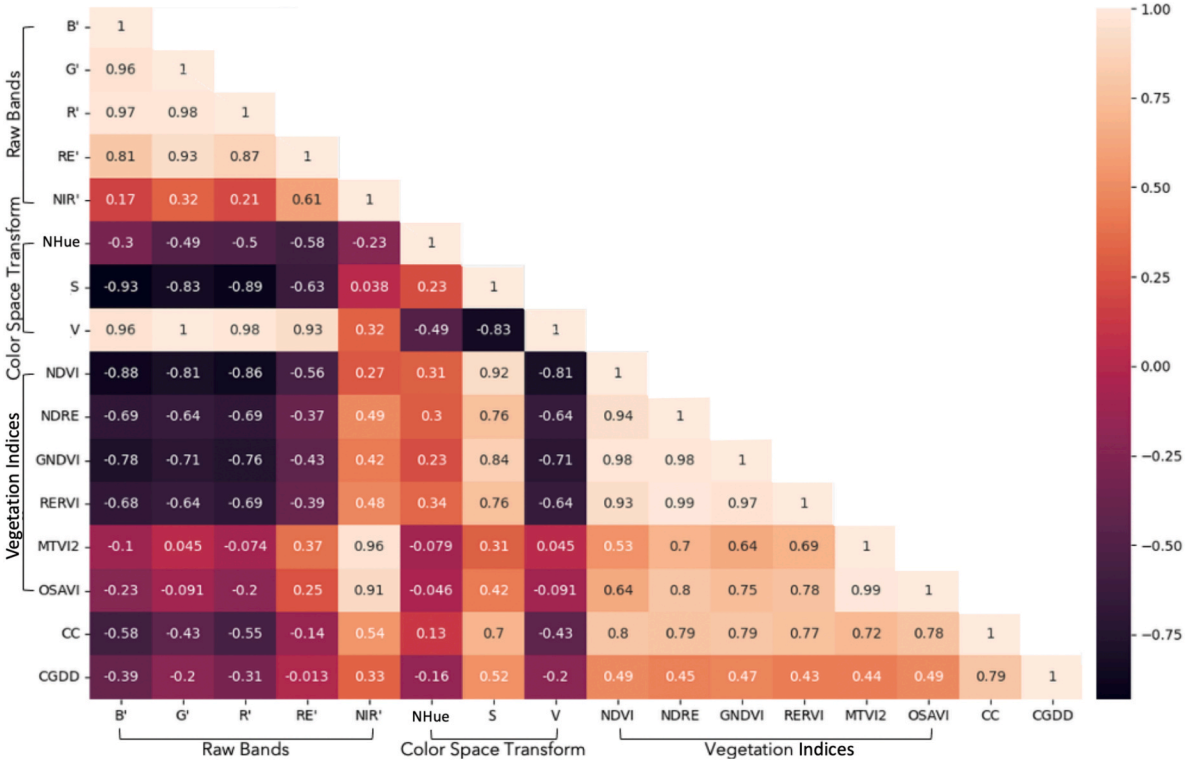

Fig. 13. Correlation heatmap illustrating relationships among all features. Strong correlations are observed among raw spectral bands and certain VIs. The inclusion of NDRE, GNDVI, and RERVI, despite their correlation, ensures a comprehensive assessment of nitrogen response in rice by capturing different aspects of chlorophyll content, canopy greenness, and biomass accumulation.

3.3. Feature selection

This study classified N levels by considering 16 features, namely 5 raw bands, 3 color space transformations, 6 VIs, CC, and CGDD. Of this set, features with predictive power were selected through RF importance, RFE, or chi-square tests. The performance of the features is comprehensively summarized in Fig. 11; the color intensity indicates the feature ranking. The best features were carefully chosen on the basis of performance.

The feature selection results revealed the key factors influencing N level classification. RERVI and CC were the most frequently selected by the methods, indicating their strong predictive power. RERVI is effective for detecting nitrogen concentrations, and CC variations are also driven by nitrogen availability. Among the VIs, GNDVI, NDRE, and OSAVI were consistently chosen. GNDVI captures chlorophyll variations, NDRE excels at revealing high nitrogen concentrations, and OSAVI mitigates soil background effects. The frequent selection of NIR′ further emphasizes the importance of NIR reflectance in nitrogen assessment.

The differences in the selected features between Periods I and II reflect differences in the phenological stages of rice growth. Period I primarily represent vegetative growth and involves changes in the canopy structure and greenness. In the reproductive stages of Period II, spectral indices with lower correlation had greater predictive power. The chi-square test, which achieved the highest OA in Period II, identified NDRE, GNDVI, RERVI, and CC as the most effective feature combination. These results underscore the importance of integrating spectral, structural, and index-based predictors for robust nitrogen classification and for guiding UAV-based monitoring strategies in precision agriculture.

The visualization results in Fig. 12 illustrate the performance of each ML model and feature selection method in predicting N levels across the two periods. The region-of-interest map represents the ground-truth classification for three N levels (L0, L1, and L2) within the experimental plots. Classification errors tended to be higher for Period I, particularly for the KNN model that included all features. Misclassification between L0 and L1 was frequent. This suggests that early-season N level classification is more challenging due to higher phenotypic variability in rice plants during the vegetative growth stage.

In Period II, classification accuracy was higher for all models and feature selection methods. The chi-square test achieved the most balanced classification results across N levels, suggesting that it can identify the most relevant features for distinguishing N levels. However, the RFE and RF importance methods also achieved competitive results. Overall, optimal feature selection methods enhanced model robustness and reduced classification errors. These methods increase the viability of UAV-based multispectral analysis for precision nitrogen management in rice fields.

Some algorithms frequently selected NIR′ and RE′ from the raw bands as critical features. The VIs used in this study were derived from NIR and RE, highlighting the relationship between nitrogen content and the high reflectance of the wavelengths at 785–899 and 705–729 nm from rice plants. The color space transformations were derived from visible-light bands and may be highly dependent on these bands, leading to potential weighting biases in a model and reducing its reliability. Fig. 13 presents the correlation heatmap for all features. Highly correlated features may be associated with dependencies. The raw bands were highly interdependent, as were RE and R. Visible light was also dependent on saturation and value. Among the VIs, OSAVI and MTVI2 were highly correlated.

The feature combinations with the highest OA for Periods I and II were selected through RFE and the chi-square test. In Period I, some features selected by RFE had high correlation. In Period II, the chi-square test identified four key features—NDRE, GNDVI, RERVI, and CC—that provided a comprehensive assessment of nitrogen status despite their correlation. Each VI captures a distinct aspect of nitrogen response: GNDVI is effective in detecting nitrogen-induced chlorophyll variations and canopy greenness, NDRE is sensitive to high chlorophyll density and leaf nitrogen content by leveraging the RE spectrum, and

RERVI provides a direct ratio of NIR to RE reflectance, which is correlated with biomass accumulation and nitrogen uptake. Their combined use minimizes the risk of overlooking critical spectral responses, ensuring a more robust nitrogen classification. The synergy among these features resulted in higher classification accuracy, and models integrating NDRE, GNDVI, RERVI, and CC outperformed those with fewer indices. This comprehensive approach improves the reliability of nitrogen assessment, supporting precise and data-driven fertilization management in rice cultivation.

4. Conclusion

This study presents a novel N level classification framework leveraging UAVs and ML to support large-scale, quantitative approaches for nutrient assessment. Rice pixel segmentation was performed by using nine spectral features and both unsupervised and supervised classification models. The ExG feature paired with the Otsu algorithm achieved a recall of 77.6 % and an OA of 79.4 % for rice plant segmentation. The DT method, trained on all nine features, had much higher performance, reaching a recall of 95.3 % and OA of 88.8 %.

In the N level classification analysis, the data were divided into Periods I and II based on key growth stages. A set of 16 spectral and structural features were used for classification. The SVM model tended to outperform the KNN model, particularly for data with nonlinear relationships. Several feature selection algorithms (RF importance, RFE, and chi-square test) were used to further refine the SVM model; the chi-square-selected features resulted in the highest OA (90.0 %) for Period II. NDRE, GNDVI, and RERVI, along with CC, were the key features with the largest contributions to classification.

CC was consistently important during vegetative growth (Period I) owing to the considerable phenotypic changes in this period. Spectral features, such as NDRE, GNDVI, and RERVI, were more influential in the reproductive stage (Period II). By selecting essential features, the model achieved robust accuracy and reliability, supporting precise, large-scale nitrogen management practices that can be implemented with automated fertilization systems, thus promoting agricultural sustainability.

However, this study has limitations. Data were collected for two crop seasons at a site, potentially restricting generalizability. Additionally, variability in rice varieties, soil types, and climatic factors may limit generalizability. UAV survey costs are currently about USD 1,200 for 10 ha; if adaptive scouting is adopted, costs could drop below USD 600, enhancing applicability (Yang et al., 2020). The high storage requirements and digitization footprint of UAV imagery was also posed challenges (Kayad et al., 2022). Future research should address these limitations by collecting diverse and extensive datasets and by strategically optimizing UAV image acquisition timing to balance data efficiency and storage demands. Additionally, incorporating time-series ML methods to capture nutrient dynamics and domain adaptation techniques (Yang et al., 2025b) will further enhance model generalizability and practical applicability in sustainable agricultural applications.

CRediT authorship contribution statement

Ming-Der Yang: Writing – review & editing, Supervision, Methodology, Funding acquisition, Conceptualization. **Yu-Chun Hsu:** Writing – review & editing, Writing – original draft, Methodology, Formal analysis, Conceptualization. **Yi-Hsuan Chen:** Writing – original draft, Software, Methodology, Formal analysis. **Chin-Ying Yang:** Visualization, Methodology, Conceptualization. **Kai-Yun Li:** Writing – original draft, Methodology.

Declaration of competing interest

The authors declare that they have no known competing financial interests or personal relationships that could have appeared to influence the work reported in this paper.

Acknowledgment

This work was partly funded by the National Science and Technology Council, Taiwan, under Grant Number NSTC113-2634-F-005-002 - Smart Sustainable New Agriculture Research Center (SMARTer).

Appendix A

Table A1
Soil chemical properties of the experimental fields. The table includes pH, phosphorus (P), potassium (K), ammonium nitrogen (NH_4^+-N), nitrate nitrogen (NO_3^--N), and available N levels in ppm. Nitrogen application rates (N Apply) are listed in kg/ha for each plot. The fields were categorized into four sections (A, B, C, D) under different nitrogen treatments (N1–N6) and irrigation practices (Conventional Planting, CP; Alternate Wetting and Drying, AWD).

Crop Season	Field	N Apply (kg/ha)	pH	P (ppm)	K (ppm)	NH_4^+-N (ppm)	NO_3^--N (ppm)	Available Nitrogen (ppm)
2020 I	A1	200	5.05	38.14	39.52	3.73	1.97	5.70
	A2	80	4.96	37.99	40.15	4.93	2.38	7.31
	A3	160	5.10	40.76	39.95	3.84	3.24	7.08
	A4	120	4.89	12.71	36.17	4.10	1.75	5.85
	B1	120	5.21	16.65	43.76	2.37	3.41	5.78
	B2	200	5.33	24.96	43.32	3.37	3.48	6.85
	B3	80	5.17	48.38	39.38	3.30	3.39	6.69
	B4	160	4.97	34.57	30.55	3.36	2.46	5.82
	C1	160	5.28	45.35	46.87	4.60	3.49	8.09
	C2	120	5.06	43.31	45.15	3.25	2.70	5.95
	C3	200	5.06	31.76	49.39	3.00	2.71	5.71
	C4	80	4.92	36.91	49.30	3.89	3.66	7.55
	D1	80	5.18	54.89	37.32	3.52	3.29	6.81
	D2	160	5.35	21.73	40.77	3.96	3.77	7.73
	D3	120	5.19	46.90	42.55	4.12	2.13	6.25
	D4	200	5.53	36.87	47.29	4.25	3.85	8.10
2020 II	A1	80	5.63	29.70	64.14	3.21	5.15	8.36
	A2	200	5.56	29.60	51.73	4.20	5.37	9.57
	A3	120	5.59	26.60	41.52	2.98	4.49	7.47

(continued on next page)

Table A1 (*continued*)

Crop Season	Field	N Apply (kg/ha)	pH	P (ppm)	K (ppm)	NH_4^+-N (ppm)	NO_3^--N (ppm)	Available Nitrogen (ppm)
	A4	160	5.82	20.39	42.10	2.24	4.36	6.60
	B1	120	5.26	40.96	39.00	3.47	2.19	5.66
	B2	80	5.16	57.46	36.91	1.89	1.93	3.82
	B3	160	5.04	46.78	38.86	2.26	2.27	4.53
	B4	200	5.22	24.87	33.18	4.81	0.62	5.43
	C1	160	5.27	60.33	41.32	4.89	1.63	6.52
	C2	120	5.33	57.65	39.42	2.67	2.30	4.97
	C3	200	5.34	53.86	38.19	2.60	2.56	5.16
	C4	80	5.56	31.15	40.36	4.32	1.20	5.52
	D1	200	5.43	69.17	38.51	1.79	2.74	4.53
	D2	160	5.35	60.17	39.58	3.65	3.44	7.09
	D3	80	5.07	44.78	35.64	4.06	3.38	7.44
	D4	120	5.39	42.16	32.69	3.19	2.14	5.33
2021 I	A1	120	5.68	55.29	48.01	2.78	10.35	13.13
	A2	140	5.71	60.42	53.79	4.75	7.25	12.00
	A3	80	5.51	66.27	57.07	2.23	11.12	13.35
	A4	200	5.58	63.54	57.59	2.06	8.66	10.72
	A5	160	5.56	52.07	61.71	3.50	8.35	11.85
	A6	100	5.46	56.34	51.83	3.21	4.11	7.32
	B1	140	5.57	44.82	55.37	4.10	2.20	6.30
	B2	200	5.53	68.69	50.21	5.18	8.42	13.60
	B3	100	5.59	68.61	60.39	3.35	6.05	9.40
	B4	120	5.59	62.05	46.34	4.50	6.66	11.16
	B5	80	5.52	53.32	49.22	4.68	4.24	8.92
	B6	160	5.28	49.45	48.40	4.16	2.85	7.01
	C1	80	5.56	60.12	52.16	4.17	4.34	8.51
	C2	140	5.71	65.26	49.51	1.54	7.37	8.91
	C3	100	5.66	64.74	52.89	2.21	6.63	8.84
	C4	160	5.45	32.43	47.36	1.69	7.71	9.40
	C5	120	5.51	31.05	52.83	1.44	8.48	9.92
	C6	200	5.42	23.29	60.83	1.14	4.10	5.24
	D1	160	5.82	31.30	48.99	3.80	6.05	9.85
	D2	120	5.85	30.08	51.94	2.38	9.87	12.25
	D3	200	5.99	30.96	51.77	2.77	8.47	11.24
	D4	100	5.86	43.24	50.02	2.58	5.18	7.76
	D5	80	6.16	53.87	45.09	2.66	6.78	9.44
	D6	140	5.78	40.36	36.46	2.70	1.53	4.23
2021 II	A1	100	5.09	33.02	55.00	3.45	4.46	7.91
	A2	160	5.04	29.83	58.17	3.44	3.81	7.25
	A3	200	5.08	30.75	61.43	4.75	8.01	12.76
	A4	80	5.05	35.42	57.79	4.70	9.28	13.98
	A5	120	5.17	23.12	58.98	6.64	4.14	10.78
	A6	140	5.17	22.61	58.47	6.93	10.65	17.58
	B1	120	4.89	27.53	75.87	4.69	7.14	11.83
	B2	80	4.91	30.13	98.56	9.79	6.86	16.65
	B3	160	5.08	27.91	74.44	5.76	3.59	9.35
	B4	100	4.75	31.56	62.97	4.08	5.49	9.57
	B5	200	4.66	17.59	67.15	6.29	6.24	12.53
	B6	140	4.57	11.87	65.74	4.76	5.59	10.36
	C1	200	5.04	27.05	59.90	5.23	9.09	14.32
	C2	120	5.10	26.04	55.97	6.65	6.23	12.89
	C3	160	5.00	24.90	80.08	6.76	17.68	24.45
	C4	80	5.08	30.71	57.71	2.48	10.25	12.74
	C5	140	4.92	20.06	62.17	3.27	5.99	9.25
	C6	100	4.85	16.04	61.40	3.71	3.77	7.48
	D1	120	5.08	38.63	68.05	5.13	17.56	22.68
	D2	100	5.40	31.36	46.27	4.54	9.63	14.17
	D3	140	5.36	30.16	49.45	4.87	9.41	14.28
	D4	200	5.30	34.17	58.92	5.23	11.20	16.43
	D5	80	5.12	24.90	61.92	4.68	9.09	13.77
	D6	160	4.69	25.40	69.05	5.83	13.79	19.63

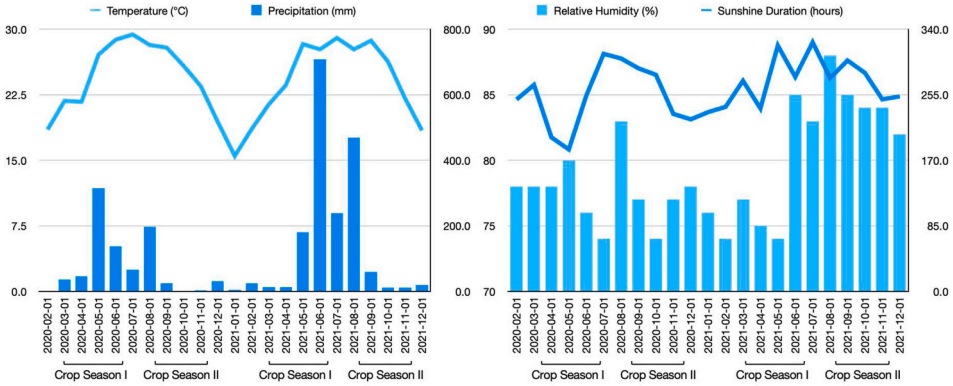

Fig. A1. Monthly climate data from February 2020 to November 2021 at G2F820 Wufeng Weather Station. The left panel shows temperature (°C, line) and precipitation (mm, bars), while the right panel presents relative humidity (%, bars) and sunshine duration (hours, line) across Crop Season I and II.

Data availability

Data will be made available on request.

References

Bagheri, N., Ahmadi, H., Alavipanah, S.K., Omid, M., 2013. Multispectral remote sensing for site-specific nitrogen fertilizer management. Pesquisa Agropecuaria Brasileira 48 (10), 1394–1401. https://doi.org/10.1590/S0100-204X2013001000011.

Bantan, R.A.R., Ali, A., Naeem, S., Jamal, F., Elgarhy, M., Chesneau, C., 2020. Discrimination of sunflower seeds using multispectral and texture dataset in combination with region selection and supervised classification methods. Chaos: Interdiscip. J. Nonlinear Sci. 30 (11). https://doi.org/10.1063/5.0024017.

Barnes, E.M., Clarke, T.R., Richards, S.E., Colaizzi, P.D., Haberland, J., Kostrzewski, M., Waller, P., Choi C., R.E., Thompson, T., Lascano, R.J., Li, H., Moran, M.S., 2000, July. Coincident detection of crop water stress, nitrogen status and canopy density using ground based multispectral data. In: Proceedings of the fifth international conference on precision agriculture, Bloomington, MN, USA, Vol. 1619, No. 6.

Barzin, R., Lotfi, H., Varco, J.J., Bora, G.C., 2022. Machine learning in evaluating multispectral active canopy sensor for prediction of corn leaf nitrogen concentration and yield. Remote Sens. (Basel) 14 (1), 1–17. https://doi.org/10.3390/rs14010120.

Brinkhoff, J., Dunn, B.W., Dunn, T., Schultz, A., Hart, J., 2025. Forecasting field rice grain moisture content using Sentinel-2 and weather data. Precis. Agric. 26 (1), 28.

Cassidy, A.P., Deviney, F.A., 2014, October. Calculating feature importance in data streams with concept drift using Online Random Forest. In: 2014 IEEE International Conference on Big Data (Big Data), pp. 23–28. IEEE. doi: 10.1109/BigData.2014.7004352.

Darst, B.F., Malecki, K.C., Engelman, C.D., 2018. Using recursive feature elimination in random forest to account for correlated variables in high dimensional data. BMC Genet. 19 (Suppl. 1), 1–6. https://doi.org/10.1186/s12863-018-0633-8.

Dutta, K., Talukdar, D., Bora, S.S., 2022. Segmentation of unhealthy leaves in cruciferous crops for early disease detection using vegetative indices and Otsu thresholding of aerial images. Measurement 189, 110478. https://doi.org/10.1016/j.measurement.2021.110478.

García Cárdenas, D.A., Ramón Valencia, J.A., Alzate Velásquez, D.F., Palacios Gonzalez, J.R., 2018. Dynamics of the indices NDVI and GNDVI in a rice growing in its reproduction phase from multi-spectral aerial images taken by drones. Adv. Intell. Syst. Comput. 893, 106–119. https://doi.org/10.1007/978-3-030-04447-3_7.

Gitelson, A.A., Kaufman, Y.J., Merzlyak, M.N., 1996. Use of the green channel in remote sensing in global vegetation for EOS-MODIS. Remote Sens. Environ. 58, 298.

Haboudane, D., Miller, J.R., Pattey, E., Zarco-Tejada, P.J., Strachan, I.B., 2004. Hyperspectral vegetation indices and novel algorithms for predicting green LAI of crop canopies: modeling and validation in the context of precision agriculture. Remote Sens. Environ. 90 (3), 337–352. https://doi.org/10.1016/j.rse.2003.12.013.

Haboudane, D., Miller, J.R., Tremblay, N., Zarco-Tejada, P.J., Dextraze, L., 2002. Integrated narrow-band vegetation indices for prediction of crop chlorophyll content for application to precision agriculture. Remote Sens. Environ. 81 (2–3), 416–426. https://doi.org/10.1016/S0034-4257(02)00018-4.

Imandoust, S.B., Bolandraftar, M., 2013. Application of K-Nearest Neighbor (KNN) approach for predicting economic events: theoretical background. Int. J. Eng. Res. Appl. 3 (5), 605–610.

Kayad, A., Sozzi, M., Paraforos, D.S., Rodrigues, F.A., Cohen, Y., Fountas, S., Francisco, M., Pezzuolo, A., Grigolato, S., Marinello, F., 2022. How many gigabytes per hectare are available in the digital agriculture era? A digitization footprint estimation. Comput. Electron. Agric. 198, 107080. https://doi.org/10.1016/j.compag.2022.107080.

Khan, S., Narvekar, M., 2022. Novel fusion of color balancing and superpixel based approach for detection of tomato plant diseases in natural complex environment. J. King Saud Univ. – Comput. Inf. Sci. 34 (6), 3506–3516. https://doi.org/10.1016/j.jksuci.2020.09.006.

Lawrence, R.L., Ripple, W.J., 1998. Comparisons among vegetation indices and bandwise regression in a highly disturbed, heterogeneous landscape: Mount St. Helens, Washington. Remote Sens. Environ. 64 (1), 91–102. https://doi.org/10.1016/S0034-4257(97)00171-5.

Lee, C.J., Yang, M.D., Tseng, H.H., Hsu, Y., Sung, Y., Chen, W.L., 2023. Single-plant broccoli growth monitoring using deep learning with UAV imagery. Comput. Electron. Agric. 207, 107739. https://doi.org/10.1109/10.1016/j.compag.2023.107739.

Li, F., Miao, Y., Feng, G., Yuan, F., Yue, S., Gao, X., Liu, Y., Liu, B., Ustin, S.L., Chen, X., 2014. Improving estimation of summer maize nitrogen status with red edge-based spectral vegetation indices. Field Crop Res. 157, 111–123. https://doi.org/10.1016/j.fcr.2013.12.018.

Li, G.S., Wu, D.H., Su, Y.C., Kuo, B.J., Yang, M.D., Lai, M.H., Lu, H.Y., Yang, C.Y., 2021. Prediction of plant nutrition state of rice under water-saving cultivation and panicle fertilization application decision making. Agronomy 11 (8), 1626. https://doi.org/10.3390/agronomy11081626.

Li, K.Y., de Lima, R.S., Burnside, N.G., Vahtmaee, E., Kutser, T., Sepp, K., Pinheiro, V.H. C., Yang, M.D., Vain, A., Sepp, K., 2022. Toward automated machine learning-based hyperspectral image analysis in crop yield and biomass estimation. Remote Sens. (Basel) 14 (5). https://doi.org/10.3390/rs14051114.

Li, S., Ding, X., Kuang, Q., Ata-UI-Karim, S.T., Cheng, T., Liu, X., Tian, Y., Zhu, Y., Cao, W., Cao, Q., 2018. Potential of UAV-based active sensing for monitoring rice leaf nitrogen status. Front. Plant Sci. 9, 1834. https://doi.org/10.3389/fpls.2018.01834.

Lin, X., Yang, F., Zhou, L., Yin, P., Kong, H., Xing, W., Lu, X., Jia, L., Wang, Q., Xu, G., 2012. A support vector machine-recursive feature elimination feature selection method based on artificial contrast variables and mutual information. J. Chromatogr. B Anal. Technol. Biomed. Life Sci. 910, 149–155. https://doi.org/10.1016/j.jchromb.2012.05.020.

Liu, Y., Feng, H., Yue, J., Fan, Y., Bian, M., Ma, Y., Jin, X., Song, X., Yang, G., 2023. Estimating potato above-ground biomass by using integrated unmanned aerial system-based optical, structural, and textural canopy measurements. Comput. Electron. Agric. 213, 108229. https://doi.org/10.1016/j.compag.2023.108229.

Liu, Y., Yang, F., Yue, J., Zhu, W., Fan, Y., Fan, J., Ma, Y., Bian, M., Chen, R., Yang, G., Feng, H., 2024. Crop canopy volume weighted by color parameters from UAV-based RGB imagery to estimate above-ground biomass of potatoes. Comput. Electron. Agric. 227, 109678. https://doi.org/10.1016/j.compag.2024.109678.

Lowe, B., Kulkarni, A., 2015. Multispectral image analysis using random forest. Int. J. Soft Comput. 6 (1), 1–14. https://doi.org/10.5121/ijsc.2015.6101.

Marinello, F., Bramley, R.G.V., Karkee, M., Cohen, Y., Fountas, S., Guo, H., Vellidis, G., 2019. Agriculture and digital sustainability: a digitization footprint. Precis. Agric. 19, 83–89. https://doi.org/10.3920/978-90-8686-888-9_9.

Meyer, G.E., Neto, J.C., 2008. Verification of color vegetation indices for automated crop imaging applications. Comput. Electron. Agric. 63 (2), 282–293. https://doi.org/10.1016/j.compag.2008.03.009.

Misra, P., Yadav, A.S., 2020. Improving the classification accuracy using recursive feature elimination with cross-validation. Int. J. Emerg. Technol. 11 (3), 659–665.

Moghimi, A., Pourreza, A., Zuniga-Ramirez, G., Williams, L.E., Fidelibus, M.W., 2020. A novel machine learning approach to estimate grapevine leaf nitrogen concentration using aerial multispectral imagery. Remote Sens. (Basel) 12 (21), 3515. https://doi.org/10.3390/rs12213515.

Orillo, J.W., Emperador, G.J., Gasgonia, M.G., Parpan, M., Yang, J., 2014, November. Rice plant nitrogen level assessment through image processing using artificial neural network. In: 2014 International Conference on Humanoid, Nanotechnology, Information Technology, Communication and Control, Environment and Management (HNICEM) (pp. 1–6). IEEE. doi: 10.1109/HNICEM.2014.7016187.

Otsu, N., 1975. A threshold selection method from gray-level histograms. Automatica 11 (285–296), 23–27.

Qiao, L., Gao, D., Zhang, J., Li, M., Sun, H., Ma, J., 2020. Dynamic influence elimination and chlorophyll content diagnosis of maize using UAV spectral imagery. Remote Sens. (Basel) 12 (16). https://doi.org/10.3390/RS12162650.

Raschka, S., Mirjalili, V., 2019. Python Machine Learning: Machine Learning and Deep Learning with Python, Scikit-learn, and TensorFlow 2. Packt Publishing Ltd.
Riehle, D., Reiser, D., Griepentrog, H.W., 2020. Robust index-based semantic plant/background segmentation for RGB-images. Comput. Electron. Agric. 169, 105201. https://doi.org/10.1016/j.compag.2019.105201.
Rouse, J.W. Jr., Haas, R.H., Schell, J.A., Deering, D.W., 1973. Monitoring the vernal advancement and retrogradation (green wave effect) of natural vegetation (No. NASA-CR-132982).
Saeys, Y., Inza, I., Larrañaga, P., 2007. A review of feature selection techniques in bioinformatics. Bioinformatics 23 (19), 2507–2517. https://doi.org/10.1093/bioinformatics/btm344.
Shao, Y.E., Dai, J.T., 2018. Integrated feature selection of ARIMA with computational intelligence approaches for food crop price prediction. Complexity 2018 (1), 1910520. https://doi.org/10.1155/2018/1910520.
Sharma, A., Deepa, R., Sankar, S., Pryor, M., Stewart, B., Johnson, E., Anandhi, A., 2021. Use of growing degree indicator for developing adaptive responses: a case study of cotton in Florida. Ecol. Ind. 124, 107383. https://doi.org/10.1016/j.ecolind.2021.107383.
Sheng, R.T.C., Huang, Y.H., Chan, P.C., Bhat, S.A., Wu, Y.C., Huang, N.F., 2022. Rice growth stage classification via RF-based machine learning and image processing. Agriculture 12 (12), 2137. https://doi.org/10.3390/agriculture12122137.
Shi, P., Wang, Y., Xu, J., Zhao, Y., Yang, B., Yuan, Z., Sun, Q., 2021. Rice nitrogen nutrition estimation with RGB images and machine learning methods. Comput. Electron. Agric. 180, 105860. https://doi.org/10.1016/j.compag.2020.105860.
Smith, A.R., 1978. Color gamut transform pairs. Comput. Graph (ACM) 12 (3), 12–19. https://doi.org/10.1145/965139.807361.
Tseng, H.H., Yang, M.D., Saminathan, R., Hsu, Y.C., Yang, C.Y., Wu, D.H., Wu, D.H., 2022. Rice seedling detection in UAV images using transfer learning and machine learning. Remote Sens. (Basel) 14 (12). https://doi.org/10.3390/rs14122837.
Tucker, C.J., 1979. Red and photographic infrared linear combinations for monitoring vegetation. Remote Sens. Environ. 8 (2), 127–150. https://doi.org/10.1016/0034-4257(79)90013-0.
Wang, J., Zhou, Q., Shang, J., Liu, C., Zhuang, T., Ding, J., Xian, Y., Zhao, L., Wang, W., Zhou, G., Tan, C., Huo, Z., 2021. UAV-and machine learning-based retrieval of wheat SPAD values at the overwintering stage for variety screening. Remote Sens. (Basel) 13 (24), 1–19. https://doi.org/10.3390/rs13245166.
Wang, Y., Hu, X., Hou, Z., Ning, J., Zhang, Z., 2018. Discrimination of nitrogen fertilizer levels of tea plant (Camellia sinensis) based on hyperspectral imaging. J. Sci. Food Agric. 98 (12), 4659–4664. https://doi.org/10.1002/jsfa.8996.
Wang, Z., Xie, Z., 2014, June. Infrared face recognition based on local binary patterns and Kruskal-Wallis test. In: 2014 IEEE/ACIS 13th International Conference on Computer and Information Science (ICIS). IEEE, pp. 185–188. doi: 10.1109/ICIS.2014.6912131.
Woebbecke, D.M., Meyer, G.E., Von Bargen, K., Mortensen, D.A., 1995. Color indices for weed identification under various soil, residue, and lighting conditions. Trans. Am. Soc. Agric. Eng. 38 (1), 259–269. https://doi.org/10.13031/2013.27838.
Wu, D.H., Chen, C.T., Yang, M.D., Wu, Y.C., Lin, C.Y., Lai, M.H., Yang, C.Y., 2022. Controlling the lodging risk of rice based on a plant height dynamic model. Bot. Stud. 63 (1). https://doi.org/10.1186/s40529-022-00356-7.
Yang, C., Wu, G., Ding, K., Shi, T., Li, Q., Wang, J., 2017. Improving land use/land cover classification by integrating pixel unmixing and decision tree methods. Remote Sens. (Basel) 9 (12). https://doi.org/10.3390/rs9121222.
Yang, C.Y., Yang, M.D., Tseng, W.C., Hsu, Y.C., Li, G.S., Lai, M.H., Wu, D.H., Lu, H.Y., 2020a. Assessment of rice developmental stage using time series uav imagery for variable irrigation management. Sensors 20 (18), 1–21. https://doi.org/10.3390/s20185354.
Yang, M.D., Hsu, Y.C., Liu, T.T., Huang, H.H., 2025a. Enhancing grain moisture prediction in multiple crop seasons using domain adaptation AI. Comput. Electron. Agric. 231, 110058.
Yang, M.D., Boubin, J.G., Tsai, H.P., Tseng, H.H., Hsu, Y.C., Stewart, C.C., 2020b. Adaptive autonomous UAV scouting for rice lodging assessment using edge. Computing with deep learning EDANet. Comput. Electron. Agric. 179, 105817. https://doi.org/10.1016/j.compag.2023.107739.
Yang, M.D., Hsu, Y.C., Tseng, W.C., Lu, C.Y., Yang, C.Y., Lai, M.H., Wu, D.H., 2021a. Assessment of grain harvest moisture content using machine learning on smartphone images for optimal harvest timing. Sensors 21 (17). https://doi.org/10.3390/s21175875.
Yang, M.D., Hsu, Y.C., Tseng, W.C., Tseng, H.H., Lai, M.H., 2025b. Precision assessment of rice grain moisture content using UAV multispectral imagery and machine learning. Comput. Electron. Agric. 230, 109813. https://doi.org/10.3390/s21175875.
Yang, M.D., Tseng, H.H., Hsu, Y.C., Yang, C.Y., Lai, M.H., Wu, D.H., 2021b. A UAV open dataset of rice paddies for deep learning practice. Remote Sens. (Basel) 13 (7). https://doi.org/10.3390/rs13071358.
Yang, M.D., Tseng, H.H., Hsu, Y.C., Tsai, H.P., 2020c. Semantic segmentation using deep learning with vegetation indices for rice lodging identification in multi-date UAV visible images. Remote Sens. (Basel) 12 (4). https://doi.org/10.3390/rs12040633.
Yang, M.D., Sykes, R.M., Merry, C.J., 2000. Estimation of algal biological parameters using water quality modeling and SPOT satellite data. Ecol. Model. 125 (1), 1–13.
Yang, W., Wang, S., Zhao, X., Zhang, J., Feng, J., 2015. Greenness identification based on HSV decision tree. Inf. Process. Agric. 2 (3–4), 149–160. https://doi.org/10.1016/j.inpa.2015.07.003.
Yang, Y., Zhao, X., Huang, M., Wang, X., Zhu, Q., 2021c. Multispectral image based germination detection of potato by using supervised multiple threshold segmentation model and Canny edge detector. Comput. Electron. Agric. 182, 106041. https://doi.org/10.1016/j.compag.2021.106041.
Yuan, Y., Wu, L., Zhang, X., 2021. Gini-impurity index analysis. IEEE Trans. Inf. Forensics Secur. 16, 3154–3169. https://doi.org/10.1109/TIFS.2021.3076932.
Zou, K., Ge, L., Zhang, C., Yuan, T., Li, W., 2019. Broccoli seedling segmentation based on support vector machine combined with color texture features. IEEE Access 7, 168565–168574. https://doi.org/10.1109/ACCESS.2019.2954587.